Accepted Manuscript

Geological Society, London, Special Publications

Effects of rotational submarine slump dynamics on tsunami-genesis – new insight from idealized models and the 1929 Grand Banks event

T. Zengaffinen, F. Løvholt, G. Pedersen & C. B. Harbitz

DOI: https://doi.org/10.1144/SP500-2019-201

Received 8 October 2019
Revised 5 December 2019
Accepted 5 December 2019

Effects of rotational submarine slump dynamics on tsunami-genesis – new insight from idealized models and the 1929 Grand Banks event

Short title: Effects of slump dynamics on tsunamis

T. Zengaffinen[1,2,*], F. Løvholt[1], G. Pedersen[2], and C. B. Harbitz[1]

[1]*Norwegian Geotechnical Institute, Sognsveien 72, 0806 Oslo, Norway*
[2]*Department of Mathematics, University of Oslo, Moltke Moes vei 35, 0851 Oslo, Norway*
[*]*Corresponding author (e-mail: thomas.zengaffinen@ngi.no)*

December 5, 2019

Abstract: Sediment slumps are known to have generated important tsunamis such as the 1998 Papua New Guinea (PNG) and the 1929 Grand Banks events. Tsunami modellers commonly use solid blocks with short run-out distances to simulate these slumps. While such methods have the obvious advantage of being simple to use, they offer little or no insight into physical processes that drive the events. The importance of rotational slump motion to tsunamigenic potential is demonstrated in this study by employing a viscoplastic landslide model with Herschel-Bulkley rheology. A large number of simulations for different material properties and landslide configurations are carried out to link the slump's deformation, rheology, its translational and rotational kinematics, to its tsunami-genesis. The yield strength of the slump is shown to be the primary material property that determines the tsunami-genesis. This viscoplastic model is further employed to simulate the 1929 Grand Banks tsunami using updated geological source information. The results of this case study suggest that the viscoplastic model can be used to simulate complex slump induced tsunami. The simulations of the 1929 Grand Banks event also indicate that a pure slump mechanism is more tsunamigenic than a corresponding translational landslide mechanism. **Keywords:** Rotational slump motion, yield strength, translational landslide kinematics, Froude number, angular momentum, tsunami-genesis, 1929 Grand Banks event

Introduction

Landslides constitute the second-most important tsunami source worldwide after earthquakes (Tappin, 2010; Harbitz et al., 2014; Yavari-Ramshe and Ataie-Ashtiani, 2016). Most recently, the 2018 Anak Krakatoa event caused several hundred fatalities (Grilli et al., 2019). Between 2007 and 2017 a string of at least five additional large sub-aerial landslides impacted water and generated run-up heights in the range of 30 m to 150 m (Sepúlveda and Serey, 2009; Wang et al., 2015; George et al., 2017; Gylfadóttir et al., 2017; Paris et al., 2019). Submarine landslide tsunamis are less frequent than these subaerial landslide tsunamis, but the largest recognized events worldwide indisputably illustrate their destructive potential and importance for society. Fatal examples of such submarine landslides are the 1998 Papua New Guinea (PNG) (Synolakis et al., 2002), 1992 Flores Island (Yeh et al., 1993), 1979 Lembata Island (Yudhicara et al., 2015), and 1929 Grand Banks landslide (Løvholt et al., 2019).

Slumps constitute a subset of landslides that are typically characterized by a rotational impulsive slope failure, a relatively coherent mass displacement, and a short landslide run-out distance. At least two of the above-mentioned events, the 1998 PNG and the 1929 Grand Banks events, were caused by rotational slumps. The study of the PNG event also led to acknowledgment in the scientific community that submarine slumps can cause large tsunamis (Bardet et al., 2003; Tappin et al., 2008). This tsunami has been successfully modelled using an approach where the landslide motion is a rigid block that follows a prescribed motion (Synolakis et al., 2002; Tappin et al., 2008), by tuning the block motion to comply with wave observations. A similar approach was adopted for modelling the slump part of the 1929 Grand Banks event (Løvholt et al., 2019). The rigid block approach was successful in these studies, because the block could mimic the rotational motion of the slump causing the tsunami-genesis in an idealized and simple way, but did not include the updated geological source information from Schulten et al. (2019b), which envisaged a slump that partly evacuated the source area. Although this block modelling approach can help to shed light on the slump motion of past events, it has several obvious shortcomings. Firstly, this method does not include landslide deformation effects that are evident from geophysical data. Secondly, these models cannot be used to take into account the landslide material properties such as the yield strength, and its effect on the landslide dynamics.

Recent modelling efforts show that the landslide rheology and deformation is important for quantifying and understanding landslide tsunami-genesis (Løvholt et al., 2017; Yavari-Ramshe and Ataie-Ashtiani, 2019). Traditionally, such landslide tsunami studies are based on translational landslide models. However, translational landslides are believed to give rise to a different generation mechanism than slumps, as they do not exhibit a rotational motion as slumps do (Løvholt et al., 2015). Until recently, slump models that include a more sophisticated deformation and rheology had not been applied for slump-induced tsunamis. Schambach et al. (2018) provided back-to-back analysis with a viscous landslide model and a rigid block model simulating slumps, with both models showing similar results. Ren et al. (2019) used a viscoplastic landslide model to generate the slump tsunami due to the 1998 PNG failure, with simulation results that compare favourably with tsunami inundation observations. These studies (Schambach et al., 2018; Ren et al., 2019) show that a slump tsunami can be effectively modelled using a landslide dynamics model. This method allows for a more flexible, general modelling treatment of the slump tsunami-genesis, including material properties, deformation, and complex topography, which will be utilized herein.

In this paper, we will use the viscoplastic model BingClaw (Løvholt et al., 2017; Kim et al., 2019), coupled to the dispersive long-wave solver GloBouss (Løvholt et al., 2008), to study slump-induced tsunamis. We will first study landslide dynamics and tsunami-genesis in an idealized geometry in one-horizontal dimension (1HD). The main aims of this idealized study are, for the first time, to:

(1) Quantify relationships between landslide material yield strength, the resulting slump kinematics and dynamics, and slump tsunamigenic potential;

(2) Identify the extent to which slump tsunamigenic potential can be attributed to translational and rotational slump kinematics, such as the angular momentum.

We will apply the same model setup in two horizontal dimensions (2HD) to study a real case, namely the 1929 Grand Banks landslide and tsunami. The main emphasis of the real case example is to ensure that the landslide parameters and settings in the idealized study can yield a realistic range of analysis. However, a detailed study of the event is left for future investigations.

The 1929 Grand Banks landslide and tsunami

On 8 November 1929 a M_w 7.2 earthquake caused a massive landslide on the Grand Banks south of Newfoundland (Heezen and Ewing, 1952; Piper et al., 1999) (see Figure 1). This submarine mass failure comprises by far the largest landslide volume ($c.$ 500 km^3) in historical time, worldwide. Deposits far from the landslide failure area and cable breaks (Heezen et al., 1954) suggest that the landslide evolved into a turbidity current. The landslide caused a several meters high tsunami at the Burin Peninsula on the south coast of Newfoundland, and waves were also recorded along the entire US East Coast, Bermuda, and the Azores (Fine et al., 2005). Initial field evidence of the landslide deposits suggested that only turbidity current masses were available in the far field (Schulten et al., 2019a). Piper et al. (1999) noted that the Grand Banks landslide was a widely distributed surficial sediment failure, and Mosher and Piper (2007) noted from newly acquired multibeam bathymetric data that there was no evidence of a massive slump failure on the St Pierre Slope. As the turbidity current itself is likely not the cause of the tsunami, it has been difficult to link the tsunami-genesis directly to landslide field evidence. Based on new field investigations of the slope failure, however, Schulten et al. (2019a) and Løvholt et al. (2019) suggested that the near field tsunami was caused by a massive slump. Løvholt et al. (2019) further hypothesised that the more widespread near-surface landslide failure as mapped by Piper et al. (1999) and Schulten et al. (2019a) caused the far-field tsunamis, and that the landslide possibly disintegrated into the turbidity current. Løvholt et al. (2019) used a simplified block source and a slump volume of 17 km^3 to model the slump. However, the analysis of newly identified faults and horizons in the St. Pierre Slope by Schulten et al. (2019b) suggest a much larger slump volume of $c.$ 390 km^3 for the primary southward slump motion. This new interpretation for the 1929 Grand Banks slump is crucial for testing whether or not our viscoplastic flow model is suited to simulate slumps. Moreover, Schulten et al. (2019b) suggest that the slump was not confined only between the structural faults containing the slump mass, but also that parts of the landslide transgressed the down-slope end of the slump source area through the channel systems, which is different from the assumption of Schulten et al. (2019a) and Løvholt et al. (2019).

Methods

Landslide model

In this paper, the viscoplastic landslide model BingClaw (Løvholt et al., 2017; Kim et al., 2019; Vanneste et al., 2019) is used to simulate the slump dynamics. The model implements the Herschel-Bulkley rheology in a two-layer depth-averaged formulation. Under simple shear conditions, the shear strain in the Herschel-Bulkley fluid is described as:

$$\left|\frac{\dot{\gamma}}{\dot{\gamma}_r}\right|^n = \begin{cases} 0, & \text{if} \quad |\tau| \le \tau_y \\ \dfrac{\tau}{\tau_y\,\mathrm{sgn}(\dot{\gamma})} - 1, & \text{if} \quad |\tau| > \tau_y \end{cases} \tag{1}$$

where $\dot{\gamma}$ is strain rate, $\dot{\gamma}_r$ a reference strain rate defined as

$$\dot{\gamma}_r = (\tau_y/\mu)^{1/n} \tag{2}$$

with dynamic consistency μ. τ and τ_y are shear stress and yield strength, respectively, and n the flow exponent. For a detailed description and derivation of the model, see Kim et al. (2019).

BingClaw solves the mass conservation equation integrated over the landslide depth (Equation 3), the momentum conservation equation integrated separately over the plug layer depth (Equation 4), and shear layer depth (Equation 5), in two horizontal dimensions (2HD). The unknown variables are bed-normal plug layer thickness d_p, bed-normal shear layer thickness d_s, plug layer volume flux per unit length $d_p\vec{v}_p$ with slope-parallel plug layer velocity $\vec{v}_p$, and shear layer volume flux per unit length $d_s\vec{v}_s$ with slope-parallel shear layer velocity $\vec{v}_s$. $d = d_p + d_s$ is the total thickness of the layers. Indices p and s indicate plug and shear layer, respectively (see Figure 2).

$$\frac{\partial}{\partial t}(d_p + d_s) + \nabla\cdot(d_p\vec{v}_p + d_s\vec{v}_s) = 0 \tag{3}$$

$$\left(1+C_m\frac{\rho_w}{\rho_d}\right)\left(\frac{\partial(d_p\vec{v}_p)}{\partial t}+\nabla\cdot(d_p\vec{v}_p\vec{v}_p)\right)+\vec{v}_p\left(\frac{\partial d_s}{\partial t}+\nabla\cdot(d_s\vec{v}_s)\right) = -g'd_p\nabla(d_p+d_s+b)-\frac{\tau_y+\tau_d}{\rho_d}\frac{\vec{v}_p}{||\vec{v}_p||} \tag{4}$$

$$\left(1+C_m\frac{\rho_w}{\rho_d}\right)\left(\frac{\partial(d_s\vec{v}_s)}{\partial t}+\nabla\cdot(\alpha d_s\vec{v}_s\vec{v}_s)\right)-\vec{v}_p\left(\frac{\partial d_s}{\partial t}+\nabla\cdot(d_s\vec{v}_s)\right)=-g'd_s\nabla(d_p+d_s+b)-\frac{\tau_y f_s}{\rho_d}\frac{\vec{v}_p}{||\vec{v}_p||} \quad (5)$$

where C_m is the added-mass coefficient, ρ_w the density of ambient water, ρ_d the density of the slump material, α the velocity form factor, and t the time coordinate. The reduced gravitational acceleration is given by $g' = g(1 - \rho_w/\rho_d)$ where g is the gravitational acceleration, b is the bathymetric depth, τ_d is the viscous drag at the free surface, split into a skin friction term τ_f given by

$$\tau_f = \frac{1}{2}C_F\rho_w\vec{v}_p||\vec{v}_p|| \quad (6)$$

and a pressure drag term τ_p given by

$$\tau_p = \frac{1}{2}C_P\rho_w\max(0, -\vec{v}_p\cdot\nabla d)\vec{v}_p \quad (7)$$

where C_F and C_P are skin friction and pressure drag coefficients, respectively, and the viscous contribution of the net shear stress at the bed is given by $\tau_y f_s$ where

$$f_s = \beta\cdot\left(\frac{||\vec{v}_p||}{\dot{\gamma}_r d_s}\right)^n.$$

β is a shape factor depending on the rheological flow exponent n (Huang and Garcia, 1998; Imran et al., 2001; Kim et al., 2019).

BingClaw combines a finite volume method for the leading order terms with a finite difference model for the source terms. The model is implemented employing the conservation law package ClawPack (Mandli et al., 2016) using the GeoClaw module (Berger et al., 2011). If the earth pressure $p = \rho_d g' d\nabla(d+b)$ does not exceed the material's shear strength in a given computational cell, no motion is imposed in that cell. Otherwise a Godunov fractional step method is used for the dynamic equations. First the equations without friction terms are solved using the finite volume method in ClawPack, then the frictional terms are accounted for the next fractional step.

Tsunami model

We use the dispersive long wave model GloBouss (Pedersen and Løvholt, 2008; Løvholt et al., 2008, 2010) to propagate the tsunami over varying bathymetry. In this study, we only use the model in linearized mode as we mainly study the tsunami in deep water, where non-linearities are not important.

When terms and factors that are not used herein are omitted (non-linear terms, Coriolis terms, spherical coordinate map-factors and dispersion enhancement terms) the hydrodynamic equations used in this paper read

$$\frac{\partial\eta}{\partial t} + \nabla\cdot(h\vec{u}) = q \quad (8)$$

$$\frac{\partial\vec{u}}{\partial t} = -\nabla\eta + \frac{1}{2}h\nabla\nabla\cdot\left(h\frac{\partial\vec{u}}{\partial t}\right) - \frac{1}{6}h^2\nabla^2\frac{\partial\vec{u}}{\partial t} \quad (9)$$

where q is a source flux term, which relates the landslide model to the tsunami model through the landslide volumetric displacement (explained below). h is the water depth relative to the mean sea surface elevation, η the sea surface elevation, and $\vec{u}$ the wave speed.

In GloBouss the equations are discretized on a staggered C-grid (Mesinger and Arakawa, 1976) in space and time to give an implicit finite difference method. An alternating direction implicit method (ADI) is used for solving the implicit algebraic equation systems for each time step. The model does not incorporate features like drying or wetting, so we cannot use this model to simulate dry-land inundation.

The slump causes a temporal volumetric change of the bathymetry, which is the primary source for the tsunami-genesis. These source fields are then run through a low pass filter that convey seabed displacements to sea surface displacements based on full potential wave theory (Kajiura, 1963; Løvholt et al., 2015) that transfers $\frac{\partial d}{\partial t}$ into $q(x, y, t)$.

Model setup

The geometrical setup is based on the most recent 1929 Grand Banks landslide information provided by Schulten et al. (2019b). Our first objective is to link a rotational slump motion to tsunami-genesis in a systematic fashion, where the slump is confined between an up-slope and a down-slope fault. To force the slump to stay between these structures, we choose to excavate the slump mass from the seabed, replace it with our viscoplastic material for the initial setup, and elevate the face of the down-slope fault (see Figure 3a,b). While we acknowledge that this geometrical description would likely differ from more complex field observations, this was a necessary simplification to force the viscoplastic material not to evacuate the structure. To this end, we first simulate the slump tsunami in one horizontal dimension (1HD). The aim is to study idealized effects of kinematics and landslide parameters on tsunami-genesis. Secondly, we study a 2HD scenario for the 1929 Grand Banks event, for which the purpose is to provide a realistic parameter range for the 1HD study.

1HD study

The 1HD geometries applied here are simplified from slope transects taken from the general Laurentian Fan bathymetry. As shown in Figure 3a,b, different bathymetries are investigated to study the sensitivity to the slope configuration of the slump source. The bathymetry outside the slump towards the shore is more gentle with a constant inclination of 0.05° in all cases.

The computational domain for the landslide model has a total length of 50 km in the x-direction with a spatial resolution of $\Delta x = 80\,\mathrm{m}$. However, due to the computational stencil of BingClaw, several cells in the azimuthal y-direction are required. Non-reflecting outflow conditions are applied at the boundaries. The Kajiura type full potential filter is run over the same length as the landslide model. Grid resolution for the Kajiura filtered output is also 80 m. For GloBouss we cover a computational domain extending 450 km horizontally, and with a resolution of 220 m. We apply a sponge layer at the right boundary, from 250 km to 450 km, that relaxes the offshore going waves (Pedersen and Løvholt, 2008). No-flux conditions are applied at the other boundaries. In GloBouss a 1HD computation involves a single wet row of cells between two dry rows of ghost cells. Spatial and temporal grid refinement tests on the landslide model BingClaw, the full potential Kajiura type filter, and the tsunami model GloBouss are described in the appendix.

Default model input parameters (i.e. density and hydrodynamic resistance) are listed in Table 1, and geometrical and geotechnical model input parameters used for the sensitivity analysis are listed in Table 2. In order to establish the list of landslide input parameters, we ran several simulations to achieve a full parameter range that spans the relevant sensitivity range for tsunami-genesis. By combining all relevant geotechnical and hydrodynamic resistance parameters for each geometrical setting, we ended up running 2640 simulations for the sensitivity analysis. We refer to 1440 model runs with constant slump volumes per unit width and variable initial slump surface slope angle as set S1, and 1440 model runs with a constant initial slump surface slope angle and variable volumes per unit width as set S2. 240 simulations overlap in set S1 and set S2.

A simplified basic geometry is defined by an initial slope angle $\theta = 2.5°$, as retrieved from the Laurentian fan, and a volume per unit width $A = 5.2\,\mathrm{km}^2$, which multiplied with a slump width of $W = 33\,\mathrm{km}$ yields a total volume $V = 175\,\mathrm{km}^3$ as suggested by Schulten et al. (2019b) for the upper part of the 1929 Grand Banks slump. Then, in simulation set S1, θ is varied between 1° and 3.5°, while keeping A constant. Likewise, in set S2, A is varied between $1.7\,\mathrm{km}^2$ and $7.5\,\mathrm{km}^2$, while keeping θ constant. In each case the parabolic shape of the rigid sea bed is adjusted accordingly.

For a very soft slump material (e.g. low values of τ_y in Table 2), the mass can be so mobile that it artificially reflects from the lower fault face and propagates back up-slope, and may even continue to slosh back and forth. This spurious sloshing occurs partly due to simplifications in the applied slump model, partly due to the geometrical setup, and partly due to too small values employed for the landslide strength. Time series of two examples of the center of mass motions, which is used to filter events, are shown in Figure 4. The center of mass velocities have a smoother time evolution than the maximum velocities. If an event gets a negative center of mass velocity, it is removed from the analysis to avoid the artificial sloshing. This criterion was based on analyses of the wave generation for the sloshing events, where it turned out that events with negative center of mass velocities influenced the wave generation significantly. An example of the artificial scaling behaviour that can be expected is discussed in one of our analysis below. The number of non-sloshing events as well as events where the yield strength is too large for the mass to mobilize the landslide (i.e. stable sediments), are shown for both set S1 and set S2 in Figure 5.

2HD study

The slump configuration with the new information provided by (Schulten et al., 2019b) is used to simulate the slump dynamics. We distinguish between two different scenarios, an over-topping (where a part of the material escape in the lower extremity) and a pure slump. For the pure slump the mass is confined to a source area limited by walls at the down-slope extremity and at the two sides. It generates a rotational slump motion in a similar way as in the 1HD study (see Figure 3c). We note that an over-topping scenario is considered as most likely by Schulten et al. (2019b) (see Figure 3d). In the case of over-topping, the model geometry is set up to allow the slide material to continue as a translational landslide outside the region of mass failure. The further disintegration into the turbidity current observed in the field is, however, not included in the model. We note that the main orientation of this slump geometry is southward, which was also assumed by Løvholt et al. (2019). Yet, the revised slump volume used in the 2HD analysis here (390 km^3) is considerably larger than what was assumed by Løvholt et al. (2019).

Model bathymetries are based on the online geographical GEBCO 2014 Grid with 463 m cell size in longitude and latitude. The depth matrix for the landslide and source computations covers a rectangle with length 114 km and 255 km in the longitudinal and latitudinal directions, respectively. For the landslide model, a grid resolution of 185 m is used, while a resolution of 463 m suffice for the surface response. As in the 1HD slump model, there is non-reflecting outflow at the four boundaries. The grid for the tsunami computations is larger and covers a rectangle of 616 km (longitude) by 555 km (latitude). It has a resolution of 463 m and includes the source area, the southern coast of Newfoundland, and the eastern coast of Nova Scotia (see Figure 1). At all four boundaries we apply a sponge layer of 22 km width where the waves are relaxed, and apply a minimum computation depth of 10 m in order to avoid spurious oscillations in shallow waters. Spatial and temporal grid refinement tests on the landslide model BingClaw, the full potential Kajiura type filter, and the tsunami model GloBouss are discussed in the appendix. Default model parameters are presented in Table 1, geotechnical and geometrical parameters are given in bold in Table 2.

Results

1HD parametric sensitivity study

Example of tsunami-genesis mechanism

We first analyse, through one single simulation, the slump tsunami-genesis mechanism. We use the following BingClaw parameters, namely $\tau_y = 70\,\text{kPa}$, $\mu = 10\,\text{kPa}\,\text{s}^n$, and $n = 0.25$. The slump surface slope angle is $\theta = 2.5°$, the slump volume per unit width is $A = 5.2\,\text{km}^2$, and the water depth of the initial center of mass is *c.* 1750 m. At *c.* 236 km from shore, a maximum vertical landslide displacement of *c.* 100 m is obtained, which is similar to what was suggested by Schulten et al. (2019b). Figure 6a shows the slump motion at different times. The corresponding generated waves at different times are displayed in Figure 6b. While the slump mass rotates around its mass center, the down-slope part of the rotational slump pushes water upwards creating a positive wave at the surface, whereas the up-slope of the slump pulls down water and causes a trough at the surface.

Next, we ran two separate simulations for the same example, one using only the positive flux part of the slump source term, and another only using the negative flux part. Figure 7 shows the generated total wave (in solid lines), as well as the wave component only due to the slump uplift (in long dashed lines), and the wave component due to the slump depression (in short dashed lines). Both the generated wave-elevations and wave-troughs continuously split into landward and offshore travelling waves as long as the slump motion continues, and add to the already propagated waves. Because the slump's upward and downward motions are spatially shifted, the landward wave-elevation travels slightly behind the landward wave-trough. Only a partial overlap of this wave-trough and wave-elevation occurs, which results in a landward trough followed by an elevation. The positive and negative amplitudes of this total wave when travelled out of the source area, are roughly half of the maximum / minimum elevations from pure positive and negative source components.

This mechanism was discussed by Løvholt et al. (2005), Haugen et al. (2005), and Løvholt et al. (2015), but mainly for translational landslides. Based on analyses of the 1998 PNG event, Løvholt et al. (2015) suggested that the interaction between rear and frontal waves were limited for slumps, and that their wave generation was more efficient than for translational landslides. However, the present analysis shows that the interaction between the frontal and rear wave clearly reduces the maximum elevation of the total wave for the 1929 Grand Banks slump. We stress that for other slump configurations and material parameters the picture could be different.

Relationship between geotechnical parameters and tsunami-genesis

Figure 8 shows the sensitivity of the maximum landward sea surface elevation η_{max} to various input parameters. η_{max} is evaluated 900 s after the slump mass release such that the wave with the highest crest has propagated out of the source area. The various input parameters include the slump material's yield strength τ_y, the volume per unit width A, the initial slump surface slope angle θ, the dynamic consistency μ, and the flow exponent n. In all cases, η_{max} is plotted as a function of τ_y, and increases consistently with decreasing τ_y. As expected, η_{max} also increases with θ and A. Furthermore, we see that η_{max} is only moderately dependent on μ. The flow exponent n has a negligible influence on tsunami-genesis, except when very small.

Relationship between landslide translational kinematics and tsunami-genesis

Figure 9 shows relationships between maximum bed-parallel and vertical slump kinematics, and maximum and absolute minimum landward sea surface elevations η_{max} and η_{min} for set S1. We recall that for S1, the initial slump surface slope angle θ is variable and the volume per unit width is constant at $A = 5.2\,\mathrm{km}^2$. The maximum kinematic quantities are calculated over the full computational domain for all times, whereas η_{max} and η_{min} are evaluated at a time of 900 s. Figure 9a shows scaled η_{max} and η_{min} as a function of the scaled maximum bed-parallel velocity $v_{||_{max}}$ and a least-square power law fit is included in some panels. η_{max} increases with $v_{||_{max}}$ following fairly well a power law behaviour with exponent of 0.9. There is more scattering for lower $v_{||_{max}}$ values. Noticing that the quantity $v_{||_{max}}/\sqrt{(gH)}$ is closely related to the Froude number (see below), we point out that the growth rate of that quantity is less than the linear Froude scaling proposed by Løvholt et al. (2015) for slumps with small Froude numbers. The linear scaling relation should exist when there is no interaction between the frontal wave-elevation and rear wave-trough. However, in this case, there is clearly a destructive interference (see Figure 7), which leads to a less effective wave generation. Figure 9c shows the relationship between the scaled maximum vertical velocity $v_{z_{max}}$, scaled η_{max} and η_{min}. Unlike in Figure 9a, we do not observe a simple power law relationship. There is also clearly more scatter in the vertical velocity plot. Further, processing of the kinematic output also verifies that maximum velocities, $v_{||_{max}}$ and $v_{z_{max}}$, and maximum accelerations, $a_{||_{max}}$ and $a_{z_{max}}$, depend strictly on each other (results not shown). Consequently, η_{max} shows a similar power law dependency on $a_{||_{max}}$ as on $v_{||_{max}}$, with an exponent of 1.01, but with a lack of a simple power law dependency on $a_{z_{max}}$ (see Figure 9b,d). The almost linear relationship with the acceleration agrees with previous investigations that heavily relied on landslide block motion (Hammack, 1973; Watts, 2000; Løvholt et al., 2005, 2015). These studies concluded that the horizontal acceleration strongly influences tsunami-genesis, and in particular, Løvholt et al. (2005, 2015) suggest the same linear relationship between η_{max} and $a_{||_{max}}$ as we find here.

We recall that set S2 has a constant initial slump surface slope angle $\theta = 2.5°$, but has different values for the volume per unit width A. The velocity is multiplied by the slump's total mass per width to quantify the momentum and to analyse how the momentum correlates with η_{max} and η_{min}. Figure 10a shows that η_{max} and η_{min} as functions of $m\,v_{||_{max}}$ follow a power law fit, however with a more gentle growth rate and more scattering for small $m\,v_{||_{max}}$ than for high $m\,v_{||_{max}}$. The exponent for η_{max} is 0.9. Figure 10c shows that η_{max} and η_{min} have a similar relationship with the vertical maximum momentum $m\,v_{z_{max}}$, but that the relationship does not follow a simple power law behaviour and with more scatter for the smallest values of the maximum vertical momentum. Figure 10b,d shows that the relationships between the rate of $m\,v_{||_{max}}$, the rate of $m\,v_{z_{max}}$, η_{max} and η_{min} follow similar relationships as the ones derived for $m\,v_{||_{max}}$ and $m\,v_{z_{max}}$, respectively. The fitted exponent between η_{max} and the rate of $m\,v_{||_{max}}$ is 1.01. For the mass times acceleration terms, we find a similar conclusion as for set S1 with a constant volume per unit width. We even remark that the power law exponents for the mass dependent terms $m\,v_{||_{max}}$ and its rate for set S2 are almost identical to the fitted power law exponents for $v_{||_{max}}$ and $a_{||_{max}}$ for set S1. However, the plots showing η_{max} and η_{min} against vertical momentum and momentum rates show less variability than the corresponding plots for η_{max} against vertical velocities and accelerations for set S1.

A Froude number, Fr, is defined as the maximum horizontal central mass velocity divided by the linear wave speed $\sqrt{gH}$ at a typical water depth $H = 2000\,\mathrm{m}$. A nearly unitary Fr means the slump's horizontal central mass speed and the tsunami speed are the same, which represents the most efficient tsunami-genesis mechanism (Løvholt et al., 2015). In our study, Fr is invariably much smaller than unity.

Figure 11 shows scaled η_{max} and η_{min} as a function of Fr for set S1, which represents the left side of the height-velocity curve peak in Figure 3 of Ward (2001). We see that the growth rate of η_{max} as a function of Fr is slower than when we use the maximum landslide velocity (i.e., in Figure 9a). On the other hand, we visually observe a slight misfit for the largest values of Fr, which may suggest that the exponent is not linear, possibly increasing with larger Fr. We note that Figure 11b also shows the results for the unfiltered simulations (i.e., including spurious sloshing events). Investigating Figure 11a,b, we see that the filter removes scenarios above $Fr \approx 0.13$. For larger Froude numbers, the scaling of the unfiltered maximum landward sea surface elevation η_{max} separates from the scaling of the absolute minimum sea surface elevation η_{min}, and the separation occurs above $Fr \approx 0.15$, say. The more rapid increase in the η_{max} with Fr is interpreted as a spurious result of the model (and hence filtered). On the other hand, we see that the scaling relationship for η_{min} is virtually unchanged for high Froude numbers (filtered events). The leading landward troughs are unaffected by the sloshing, which hints that a linear Froude scaling should also be expected for somewhat larger Froude numbers than those analysed elsewhere in this paper.

Relationship between landslide rotational kinematics and tsunami-genesis

Slumps are mainly rotational and display different kinematics compared to translational landslides with long run-out. Here, we analyse to which extent the slump's scaled maximum angular momentum L_{max} is attributed to the slump's tsunamigenic potential. The technical derivation of this quantity is given in the appendix. Figure 12a shows a power law relationship between L_{max}, η_{max} and η_{min} for set S1. The exponent for η_{max} is 0.76. Figure 12b shows that the dependency between L_{max}, η_{max} and η_{min} for set S2 has significantly more scatter, and a less clear correlation. The fitted exponent is 0.66 for η_{max}. In both cases, the data exhibit little scatter for large L_{max}.

2HD study related to the 1929 Grand Banks event

Slump scenarios with over-topping

Figure 13 shows the simulated motion of the slump with over-topping for a volume of $V = 390\,\mathrm{km}^3$ and a yield strength of $\tau_y = 85\,\mathrm{kPa}$. At 300 s, the slump is still confined in the fault structure. Around $t = 600\,\mathrm{s}$ the slump has its maximum vertical uplift of *c.* 400 m at its down-slope extremity while parts of the slump mass escape the faulted pit and continue down-slope as a translational landslide. This over-topping results in a 100 m high frontal landslide height. The output at 1380 s shows the landslide flowing into the Laurentian Fan region.

In the early phase, the generated wave (see Figure 14) has a positive sea surface elevation at the southern end of the slump area and a negative elevation at the northern end of the slump area. It is aligned NS along the failure surface slope orientation. One hour after the slump mass release, the wave has started to turn gradually northwards and reaches the latitude 46° N after two hours. The main wave direction is towards the Burin Peninsula, whereas there is also focusing towards the Avalon Peninsula further east. Results extracted over the transect just south of Burin further show that maximum offshore sea surface elevations range from 4 m to 9 m for different landslide yield strengths (see Figure 15a), which are in the same range or, for the lowest yield strengths, somewhat higher than those found by Løvholt et al. (2019). Figure 16a shows the maximum sea surface elevations over the full simulation time, which coincides with the large waves observed near the Burin Peninsula (see e.g. Fine et al. (2005)). Field observations of run-up elsewhere were mostly below 2 m, however, our simulations show as large waves near Nova Scotia and the Avalon Peninsula as near Burin.

More tuning would be necessary to provide a closer agreement with the data. For instance, Schulten et al. (2019b) found a vertical uplift of the slump mass of 100 m at its down-slope extremity, although our example with $\tau_y = 85\,\mathrm{kPa}$ produces a much larger vertical uplift of *c.* 400 m. Our simulations merely provide a first attempt. However, the simulations clearly show that the viscoplastic model is capable of producing sufficiently strong slump induced waves to produce a tsunami at least of the size of the 1929 Grand Banks event. We re-emphasise that our objective here was primarily to investigate whether the material parameter ranges for the 1HD case were representative for a real example, and this analysis shows that they are.

Slump scenarios without over-topping

We turn our attention to the pure slump, which is confined by the outreaching fault at the lower extremity, and to its tsunami using the same volume and material parameters as for the over-topping slump. Figure 17 shows the slump thickness 0 s, 300 s, 600 s, and 840 s after the mass release. At the last time the slump motion has stopped. The maximum vertical uplift is *c.* 800 m, which is twice as much as for the over-topping slump due to the confinement. The spreading waves (see Figure 18) and the total wave field (see Figure 16b) have a similar radiation pattern as the over-topping slump tsunami, however, the positive generated waves are significantly larger along the ridges between the Laurentian Channel, the Halibut Channel, and the Haddock Channel than the waves for the over-topping slump source (see Figure 16). Figure 15b shows a transect just south of Burin with maximum offshore sea surface elevations ranging from 1 m to 5 m, which are, however, in the same range as the sea surface elevations for the over-topping case. Near the 55.7° longitude, we see that the over-topping scenario produces slightly larger waves than the pure slump. Still, on an overall basis, we suggest that the pure slump event seems to be a slightly more efficient tsunami generator than the over-topping event. This was confirmed by own preliminary work on simulating Grand Banks (results not shown) with other slump configurations, where the difference was even clearer.

Concluding remarks

In this paper, we have conducted a study of slump-induced tsunamis using a depth-averaged viscoplastic landslide model as the tsunami source, and a linear dispersive long-wave model for the tsunami propagation. Our main emphasis has been to study the sensitivity to slump material properties in one-horizontal dimension (1HD) on idealized geometries and the resulting slump kinematics on tsunami-genesis. Contrary to most previous studies, our use of a viscoplastic landslide model allows us to link the tsunami directly to slump material properties, and avoid ad-hoc assumptions commonly made using a block model approach where the slump motion is prescribed. This refined model allows a more generalized treatment of slump sources, and hence is not limited to models that retrofit block source properties to simulate past events.

This study has shown that the material parameter that influences tsunami-genesis the most is the initial yield strength of the sediment. Similar conclusions were reached for translational landslides in studies of the tsunami-genesis for the Storegga landslide, for example (Kim et al., 2019). Moreover, our range of the dynamic landslide consistency (related to the viscosity) shows a more moderate influence on tsunami-genesis. Naturally, geometrical factors such as the slope angle and volume of the slump were found to have a strong influence on the tsunami-genesis too. Several kinematic properties were found to correlate well with the maximum landward sea surface elevation. For the case of constant slide volume, the maximum landward sea surface elevation increases monotonically with both scaled bed-parallel maximum velocity and acceleration mimicking a power law relationship. The maximum landward sea surface elevation also increases monotonically with vertical acceleration and velocity, but a less systematic relationship was found in this case. For the more general cases where variable volumes were investigated, the maximum bed-parallel momentum and momentum rates correlate well with the maximum landward sea surface elevation, while the maximum landward sea surface elevation had a somewhat less systematic relationship with corresponding vertical momentum and momentum rates.

Some of the findings of this study have been identified already in past studies (Ward, 2001; Tinti et al., 2001; Løvholt et al., 2005), but only for translational landslides with a simplified block source representation. Here, we show that similar relationships between landslide velocities, accelerations, and momentum apply for slumps. In particular, we find the scaling between the maximum height of the generated wave and the maximum bed-parallel landslide speed divided by the wave celerity, $\eta_{max} \propto Fr^{0.9}$. We note that the exponent of 0.9 is less than the linear relationship (i.e. exponent 1) expected for small Froude numbers for frontal wave elevations and rear wave troughs without any interference (Løvholt et al., 2015). In our study, we clearly have destructive interference between the waves caused at the front and rear part of the slump which reduced the tsunamigenic potential. However, we find, similar to Løvholt et al. (2005, 2015), an almost linear scaling with the horizontal landslide acceleration, which is hence clearly a good proxy for the tsunamigenic potential. An additional finding from our study is that the angular momentum shows a particularly good correlation with the maximum landward sea surface elevation. This suggests that the tsunamigenic potential can be directly linked to rotational kinematic properties of the slump. We are unaware of previous studies that identify such a relationship.

A second part of the study is devoted to studying the 1929 Grand Banks slump and tsunami in a real topographical setting. This was primarily done to investigate whether the parameter ranges used in the viscoplastic slump model in 1HD were realistic. A detailed analysis of the 1929 Grand Banks event with emphasis of obtaining a close match with field observations of the tsunami was not attempted. Nevertheless, our model was set up with new field observations by Schulten et al. (2019b) to illustrate how the geological interpretation provided a significantly revised explanation for the slump event. Schulten et al. (2019b) concluded that the 1929 Grand Banks slump failed mainly southwards, and that the main slump volume was much larger than previously thought (390 km^3). Our tsunami modelling suggests that a viscoplastic model indeed should be capable of producing sufficiently large waves. The 1929 Grand Bank event also served the purpose of testing how a complex event with slump failure and over-topping compares with a pure slump event with respect to tsunami-genesis. We found that the pure slump produced larger overall waves compared to the over-topping scenario. All in all, the 1929 Grand Banks model including new field observations for the slump event and an idealized study in one-horizontal dimension could revise our understanding of tsunami-genesis.

Acknowledgements

Computations were done on a computer located at the Norwegian Geotechnical Institute in Oslo, Norway. This project has received funding from the European Union's Horizon 2020 research and innovation programme under the Marie Sklodowska-Curie grant agreement No. 721403. The authors are very grateful for positive criticism from the editor Aggeliki Georgiopoulou, and the reviewers David Mosher and Alberto Armigliato.

Appendix

Grid refinement tests

For the 1HD simulations, we conducted grid refinement tests on the spatial grid for the slump model, tsunami model, and the Kajiura type filter (resolutions and parameters in Table 3). For the slump model, we tested soft slump materials, low τ_y and low μ. The slump thickness depended strongly on the grid resolution for $\Delta x > 80$ m. After 240 s, for instance, the slump thickness at the lower extremity is 8% thinner for $\Delta x = 160$ m than for $\Delta x = 26$ m, and for resolutions $\Delta x \leq 80$ m, the slump thickness varies maximum by 4%. The slump thickness at the up-slope part coincides for resolutions $\Delta x \leq 80$ m, but gives twice the corresponding slump thickness for $\Delta x = 160$ m. Thus a spatial grid resolution of 80 m is chosen for further use. The time step, Δt, is adapted during the simulation to keep the Courant-Friedrichs-Lewy number (Courant et al., 1967),

$$\mathrm{CFL} = \frac{U_o \, \Delta t}{\Delta x}, \tag{10}$$

constant. Here U_o is the maximum particle speed in the slide body. In all our 1HD model runs, we use a CFL= 0.45, which yields stable behaviour (greatest landslide velocities are *c.* 70 m s^{-1}). When the source input is fed into the tsunami model each 30 s, we have a deviation of less than 2% from the smallest interval tested (5 s) at $t = 480$ s. Hence, we stay with 30 s. Since the surface response is smoother than the slide surface, application of the same spatial grid resolution for the Kajiura type filter as for the landslide model, 80 m, is more than adequate. We tested spatial grid resolutions for the tsunami model 980 s after slump mass release. The maximum landward sea surface elevation of a resolution of 220 m only deviated by 0.6% from the elevation of a finer resolution of 55 m. Therefore, we further used the 220 m resolution. The CFL number used is 0.5.

In 2HD, we executed spatial and temporal grid refinement tests of the landslide model BingClaw, the Kajiura type filter, and the tsunami model GloBouss. All numerical parameters can be found in Table 4. For BingClaw we evaluated the grid dependency on the slump thickness after 600 s in a transect striking NS. At the location of the thickest slump mass, the thickness obtained with $\Delta x = 185$ m deviated only by 1.7% from that of $\Delta x = 93$ m. The double the resolution of 370 m caused a corresponding deviation of 6.8%. Thus we used a spatial resolution of 185 m. The slump was stable with a CFL number of 0.65.

We evaluated the spatial resolution of the input fluxes into GloBouss 120 s after failure by analysing the first wave amplitudes of the propagated waves along the same transect striking NS. The wave height of the 926 m resolution differed only by 3.1% from that of 232 m. However, since it was feasible to use even 463 m in the modeling, we chose that. These sources were fed into GloBouss at various time intervals (see Table 4), whereas the resulting wave field 3000 s after failure was analysed. The amplitude of a resolution of 50 s deviated by 8% from a 30 s resolution. The wave amplitude of a finer resolution of 20 s deviated by 2% from the 30 s resolution. Thus the flux sources were fed into GloBouss each 30 s.

We tested three spatial grid resolutions for the tsunami propagation model GloBouss 4100 s after failure. The first wave amplitude of the second finest resolution deviated 2% from the finest resolution, and the coarsest resolution deviated by 8% from the finest resolution. Since the finest resolution was feasible we applied that one. The CFL number in GloBouss was chosen as 0.8.

Kinematics

As we run our models in a depth-averaged regime, we divide the slump mass into vertical columns with length of one cell size. The height difference of the slump surface H in each column at two adjacent time steps serves as input for the vertical velocity calculation. With that velocity we calculate the vertical acceleration a_z in each column. It should be noted that resulting vertical velocities are half a time step behind the time of the surface heights of the next time loop, and the vertical accelerations are half a time step behind the velocities. The actual calculation of the vertical acceleration is a central derivative:

$$a_z^{(n)} = \frac{H^{(n+1)} - 2H^{(n)} + H^{(n-1)}}{\Delta t^2} \qquad \text{for} \quad n \geq 2 \tag{11}$$

The first calculated acceleration refers to $t^{(n=1)} = 0.25\Delta t$, which means that the time interval for the calculations Δn is not constant for $t < \Delta t$.

Another kinematic quantity is the bed-parallel acceleration $a_{||}$, evaluated at the same time. In order to do so, we need to average the bed-parallel velocity $u_{||}$ between two time steps and then evaluate the time derivative:

$$a_{||}^{(n)} = \frac{\frac{v_{||}^{(n+1)} + v_{||}^{(n)}}{2} - \frac{v_{||}^{(n)} + v_{||}^{(n-1)}}{2}}{\Delta t} \qquad \text{for} \quad n \geq 2 \tag{12}$$

The same exception for the first calculation step $n = 1$ applies here.

A third quantity is the angular momentum $\vec{L}$ of the entire slump mass, which is defined as $d\vec{L} = m(\vec{r} \times \vec{v})$ where m is the mass of a vertical column, $\vec{r}$ the position vector, and $\vec{v}$ the velocity vector. Each quantity is time dependent. The position vector ranges from the dynamic center of mass to the average center of a vertical column between two time steps. Position and velocity vectors are both split into horizontal and vertical components, r_x and r_z, v_x and v_z, respectively. The vertical velocity component corresponds to the one from the calculations above, but we approximate the horizontal velocity component v_x with the bed-parallel velocity $v_{||}$, as the bed is nearly horizontal. Maximum bed slope angle is 5.25°. Equation 13 shows the calculation for the total angular momentum, which is a sum of all angular momenta for each vertical column.

$$\vec{L}^{(n-\frac{1}{2})} = \sum_{n=1}^{n_{end}} m \frac{\vec{r}^{(n)} + \vec{r}^{(n-1)}}{2} \times \frac{\vec{u}^{(n)} + \vec{u}^{(n-1)}}{2} = \sum_{n=1}^{n_{end}} m \left(r_x^{(n-\frac{1}{2})} v_z^{(n-\frac{1}{2})} - r_z^{(n-\frac{1}{2})} v_{||}^{(n-\frac{1}{2})} \right) \tag{13}$$

For the analysis in this study, we use maximum values of all times of each quantity described above.

References

Bardet, J.-P., Synolakis, C., Davis, H., Imamura, F., and Okal, E. (2003). Landslide tsunamis: Recent findings and research directions. *Pure and App. Geophys.*, 160:1793–1809.

Berger, M. J., George, D. L., LeVeque, R. J., and Mandli, K. T. (2011). The GeoClaw software for depth-averaged flows with adaptive refinement. *Adv. Water Res.*, 34:1195–1206.

Courant, R., Friedrichs, K., and Lewy, H. (1967). On the partial difference equations of mathematical physics. *IBM Journal of Research and Development*, 11(2):215–234.

Fine, I., Rabinovich, A., Bornhold, B., Thomson, R., and Kulikov, E. (2005). The Grand Banks landslide-generated tsunami of November 18, 1929: preliminary analysis and numerical modeling. *Marine Geology*, 215(1-2):45–57.

George, D., Iverson, R., and Cannon, C. (2017). New methodology for computing tsunami generation by subaerial landslides: Application to the 2015 Tyndall Glacier landslide, Alaska. *Geophysical Research Letters*, 44(14):7276–7284.

Grilli, S. T., Tappin, D. R., Carey, S., Watt, S. F., Ward, S. N., Grilli, A. R., Engwell, S. L., Zhang, C., Kirby, J. T., Schambach, L., et al. (2019). Modelling of the tsunami from the December 22, 2018 lateral collapse of Anak Krakatau volcano in the Sunda Straits, Indonesia. *Scientific reports*, 9(1):11946–11946.

Gylfadóttir, S. S., Kim, J., Helgason, J. K., Brynjólfsson, S., Höskuldsson, Á., Jóhannesson, T., Harbitz, C. B., and Løvholt, F. (2017). The 2014 Lake Askja rockslide-induced tsunami: Optimization of numerical tsunami model using observed data. *Journal of Geophysical Research: Oceans*, 122(5):4110–4122.

Hammack, J. L. (1973). A note on tsunamis: their generation and propagation in an ocean of uniform depth. *Journal of Fluid Mechanics*, 60(4):769–799.

Harbitz, C., Løvholt, F., and Bungum, H. (2014). Submarine landslide tsunamis: how extreme and how likely? *Nat. Haz.*, 72(3):1341–1374.

Haugen, K. B., Løvholt, F., and Harbitz, C. B. (2005). Fundamental mechanisms for tsunami generation by submarine mass flows in idealised geometries. *Marine and Petroleum Geology*, 22(1-2):209–217.

Heezen, B. C., Ericson, D., and Ewing, M. (1954). Further evidence for a turbidity current following the 1929 Grand Banks earthquake. *Deep Sea Research (1953)*, 1(4):193–202.

Heezen, B. C. and Ewing, W. M. (1952). Turbidity currents and submarine slumps, and the 1929 Grand Banks [Newfoundland] earthquake. *American journal of Science*, 250(12):849–873.

Huang, X. and Garcia, M. H. (1998). A Herschel-Bulkley model for mud flow down a slope. *Journal of fluid mechanics*, 374:305–333.

Imran, J., Parker, G., Locat, J., and Lee, H. (2001). 1D numerical model of muddy subaqueous and subaerial debris flows. *Journal of hydraulic engineering*, 127(11):959–968.

Kajiura, K. (1963). The leading wave of a tsunami. *Bulletin of the Earthequake reserch Institue*, 41:535–571.

Kim, J., Løvholt, F., Issler, D., and Forsberg, C. F. (2019). Landslide Material Control on Tsunami Genesis-The Storegga Slide and Tsunami (8,100 Years BP). *Journal of Geophysical Research: Oceans*.

Løvholt, F., Bondevik, S., Laberg, J. S., Kim, J., and Boylan, N. (2017). Some giant submarine landslides do not produce large tsunamis. *Geophysical Research Letters*, 44(16):8463–8472.

Løvholt, F., Harbitz, C. B., and Haugen, K. B. (2005). A parametric study of tsunamis generated by submarine slides in the Ormen Lange/Storegga area off western Norway. *Marine Petroleum and Geology*, 22:219–231.

Løvholt, F., Pedersen, G., and Gisler, G. (2008). Oceanic propagation of a potential tsunami from the La Palma Island. *Journal of Geophysical Research: Oceans*, 113(C9).

Løvholt, F., Pedersen, G., Harbitz, C. B., Glimsdal, S., and Kim, J. (2015). On the characteristics of landslide tsunamis. *Phil. Trans. R. Soc. A*, 373(2053):20140376.

Løvholt, F., Pedersen, G. K., and Glimsdal, S. (2010). Coupling of dispersive tsunami propagation and shallow water coastal response. *Open Oceanography Journal, Caribbean Waves Special Issue*, 4:71–82.

Løvholt, F., Schulten, I., Mosher, D., Harbitz, C., and Krastel, S. (2019). Modelling the 1929 Grand Banks slump and landslide tsunami. In *Subaqueous Mass Movements*, volume 477 of *Special Publications*. The Geological Society of London.

Mandli, K. T., Ahmadia, A. J., Berger, M., Calhoun, D., George, D. L., Hadjimichael, Y., Ketcheson, D. I., Lemoine, G. I., and LeVeque, R. J. (2016). Clawpack: building an open source ecosystem for solving hyperbolic PDEs. *PeerJ Computer Science*, 2:e68.

Mesinger, F. and Arakawa, A. (1976). Numerical methods used in atmospheric models. *Global Atmospheric Research Programme (GARP)*, 64(17).

Mosher, D. C. and Piper, D. J. (2007). Analysis of multibeam seafloor imagery of the Laurentian Fan and the 1929 Grand Banks landslide area. In *Submarine mass movements and their consequences*, pages 77–88. Springer.

Paris, A., Okal, E. A., Guérin, C., Heinrich, P., Schindelé, F., and Hébert, H. (2019). Numerical modeling of the June 17, 2017 landslide and tsunami events in Karrat Fjord, West Greenland. *Pure and Applied Geophysics*, pages 1–23.

Pedersen, G. and Løvholt, F. (2008). Documentation of a global Boussinesq solver. *Preprint series. Mechanics and Applied Mathematics http://urn. nb. no/URN: NBN: no-23418*.

Piper, D. J., Cochonat, P., and Morrison, M. L. (1999). The sequence of events around the epicentre of the 1929 Grand Banks earthquake: initiation of debris flows and turbidity current inferred from sidescan sonar. *Sedimentology*, 46(1):79–97.

Ren, Z., Zhao, X., and Liu, H. (2019). Numerical study of the landslide tsunami in the South China Sea using Herschel-Bulkley rheological theory. *Physics of Fluids*, 31(5):056601.

Schambach, L., Grilli, S. T., Kirby, J. T., and Shi, F. (2018). Landslide Tsunami Hazard Along the Upper US East Coast: Effects of Slide Deformation, Bottom Friction, and Frequency Dispersion. *Pure and Applied Geophysics*, pages 1–40.

Schulten, I., Mosher, D. C., Krastel, S., Piper, D. J., and Kienast, M. (2019a). Surficial sediment failures due to the 1929 Grand Banks Earthquake, St Pierre Slope. In *Subaqueous Mass Movements*, volume 477 of *Special Publications*. The Geological Society of London.

Schulten, I., Mosher, D. C., Piper, D. J., and Krastel, S. (2019b). A massive slump on the St. Pierre Slope, a new perspective on the 1929 Grand Banks submarine landslide. *Journal of Geophysical Research: Solid Earth*.

Sepúlveda, S. A. and Serey, A. (2009). Tsunamigenic, earthquake-triggered rock slope failures during the April 21 2007 Aisén earthquake, southern Chile (45.5° S). *Andean Geol.*, 26(1):131–136.

Synolakis, C. E., Bardet, J.-P., Borrero, J. C., Davies, H. L., Okal, E. A., Silver, E. A., Sweet, S., and Tappin, D. R. (2002). The slump origin of the 1998 Papua New Guinea tsunami. *Proceedings of the Royal Society of London. Series A: Mathematical, Physical and Engineering Sciences*, 458(2020):763–789.

Tappin, D. (2010). Mass transport events and their tsunami hazard. In *Submarine Mass Movements and Their Consequences*, volume 28 of *Adv. Nat. Technol. Haz. Res.*, pages 667–684. Springer Science.

Tappin, D. R., Watts, P., and Grilli, S. T. (2008). The Papua New Guinea tsunami of 17 July 1998: Anatomy of a catastrophic event. *Nat. Haz. Earth Sys. Sci.*, 8:243–266.

Tinti, S., Bortolucci, E., and Chiavettieri, C. (2001). Tsunami excitation by submarine slides in shallow-water approximation. *Pure and Applied Geophysics*, 158(4):759–797.

Vanneste, M., Løvholt, F., Issler, D., Liu, Z., Boylan, N., Kim, J., et al. (2019). A Novel Quasi-3D Landslide Dynamics Model: From Theory to Applications and Risk Assessment. In *Offshore Technology Conference*. Offshore Technology Conference.

Wang, J., Ward, S. N., and Xiao, L. (2015). Numerical simulation of the December 4, 2007 landslide-generated tsunami in Chehalis Lake, Canada. *Geophysical Journal International*, 201(1):372–376.

Ward, S. N. (2001). Landslide tsunami. *Journal of Geophysical Research*, 6:11,201–11,215.

Watts, P. (2000). Tsunami features of solid block underwater landslides. *Journal of waterway, port, coastal, and ocean engineering*, 126(3):144–152.

Yavari-Ramshe, S. and Ataie-Ashtiani, B. (2016). Numerical modeling of subaerial and submarine landslide-generated tsunami waves-recent advances and future challenges. *Landslides*, 13(6):1325–1368.

Yavari-Ramshe, S. and Ataie-Ashtiani, B. (2019). On the effects of landslide deformability and initial submergence on landslide-generated waves. *Landslides*, 16(1):37–53.

Yeh, H., Imamura, F., Synolakis, C., Tsuji, Y., Liu, P., and Shi, S. (1993). The Flores island tsunamis. *Eos, Transactions American Geophysical Union*, 74(33):369–373.

Yudhicara, Bani, P., and Darmawan, A. (2015). Geothermal System as the Cause of the 1979 Landslide Tsunami in Lembata Island, Indonesia. *Indonesian Journal on Geoscience*, 2(2):91–99.

List of Figures

Fig. 1 Bathymetric map of the computational domain for the 2HD tsunami simulations. The bathymetry inside the large red rectangle is used for the simulation of the 2HD landslide dynamics and the small red rectangle is the slump source area. The red line just south of the Burin Peninsula represents the transect that is used to extract simulation results shown in Figure 15. The red cross shows the epicenter of the M_w 7.2 earthquake on 8 November 1929. 16

Fig. 2 Simplified schematic plot of the velocity profile (**a**) before and (**b**) during the slump motion simulated with the depth-averaged BingClaw model (modified after Kim et al. (2019) for our slump model). The velocity profile is uniform in the plug layer, but follows a power-law with exponent $n+1$ in the bottom shear layer. Velocities v_p and v_s, and thicknesses d_p and d_s vary spatially and temporally. 16

Fig. 3 Initial 1HD bathymetry with slump masses for (**a**) set S1 and (**b**) set S2. Bathymetry with orange lines indicate the same geometrical setup. Transects through longitude $-55.77°$ over the initial 2HD bathymetry for (**c**) the pure slump that includes side walls and a bottom wall, and (**d**) the over-topping slump. The orange line indicates the initial slump surface and the blue line the seabed for the simulations. The green line represents the seabed surface prior to excavation. 17

Fig. 4 Time series of center of mass velocity $v_{x,centre}$ and peak bed-parallel velocity over the entire slump body $v_{||,peak}$. Maximum velocities are used for further analyses. Employed parameters are $\mu = 10\,\mathrm{kPa\,s}^n$, $n = 0.25$, the slump surface slope angle is $\theta = 2.5°$, the slump volume per unit width is $A = 5.2\,\mathrm{km}^2$, and (**a**) $\tau_y = 70\,\mathrm{kPa}$, (**b**) $\tau_y = 40\,\mathrm{kPa}$. 18

Fig. 5 Number of non-sloshing events and events with velocities greater than zero as a function of yield strength τ_y, (**a**) initial slump surface slope angle θ and (**b**) slump volume per unit width A. All combinations of flow exponent n and dynamic viscosity μ combine to a total of 30 events. Low τ_y, large A, and large θ indicate sloshing events. Large τ_y, low A, and low θ indicate stable sediments and are coloured in green. 18

Fig. 6 (**a**) Simulated submarine slump shown for different times. The employed BingClaw parameters are $\tau_y = 70\,\mathrm{kPa}$, $\mu = 10\,\mathrm{kPa\,s}^n$, $n = 0.25$, the slump surface slope angle is $\theta = 2.5°$, and the slump volume per unit width is $A = 5.2\,\mathrm{km}^2$. We show the slump from its initial state until it stops moving, 1200 s after failure. The dots indicate the center of mass of the slump as a function of time; (**b**) tsunami-genesis and propagation until 900 s, which is the time we evaluate the maximum and absolute minimum landward sea surface elevation. The offshore going wave has been relaxed by the sponge layer at the right boundary starting at 250 km from the shore. 19

Fig. 7 Tsunami split into the total wave (in solid lines), due to slump uplifts (in long dashed lines) and slump depressions (in short dashed lines). Elapsed times are (**a**) 300 s and (**b**) 900 s. The latter time is when we evaluate the maximum and absolute minimum landward sea surface elevation. The offshore going wave has been relaxed by the sponge layer at the right boundary starting at 250 km from the shore. 19

Fig. 8 Maximum landward sea surface elevations η_{max} as a function of yield strength τ_y for a selection from (**a**) set S1, (**b**) set S2, and (**c**,**d**) common scenarios from both sets. Orange lines in all subplots refer to the same scenarios. Fixed parameters (except where parameters are subject to variation) are $\mu = 10\,\mathrm{kPa\,s}^n$, $n = 0.25$, $\theta = 2.5°$, and $A = 5.2\,\mathrm{km}^2$. 20

Fig. 9 Scaled maximum and absolute minimum landward sea surface elevation η_{max} and η_{min} against (**a**) scaled maximum bed-parallel slump velocity $v_{||_{max}}$, (**b**) scaled maximum bed-parallel slump acceleration $a_{||_{max}}$, (**c**) scaled maximum vertical slump velocity $v_{z_{max}}$, and (**d**) scaled maximum vertical slump acceleration $a_{z_{max}}$ for set S1. The scale for the sea surface elevation is the typical water depth $H = 2000\,\mathrm{m}$, the velocity scale is the linear wave speed $\sqrt{gH}$, and the acceleration scale is the square linear wave speed $\sqrt{gH}$ divided by the typical slump thickness $d = 250\,\mathrm{m}$. The power law fits apply to η_{max} with x representing the x-axes. 21

Fig. 10 Scaled maximum and absolute minimum landward sea surface elevation η_{max} and η_{min} against (**a**) scaled maximum bed-parallel slump momentum $m\,v_{||_{max}}$, (**b**) scaled maximum bed-parallel slump momentum rate $m\,a_{||_{max}}$, (**c**) scaled maximum vertical slump momentum $m\,v_{z_{max}}$, and (**d**) scaled maximum vertical slump momentum rate $m\,a_{z_{max}}$ for set S2. The scale for the sea surface elevation is the typical water depth $H = 2000\,\mathrm{m}$, the momentum scale is the largest mass M (from the $A = 7.5\,\mathrm{km}^2$ scenarios) times the linear wave speed $\sqrt{gH}$, and the scale for the momentum rate is the largest mass M times the square linear wave speed $\sqrt{gH}$ divided by the typical slump thickness $d = 250\,\mathrm{m}$. The power law fits apply to η_{max} with x representing the x-axes. 22

Fig. 11 Scaled maximum and absolute minimum landward sea surface elevation η_{max} and η_{min} as a function of the Froude number Fr for set S1, with (**a**) filtered events only and (**b**) unfiltered events with dots representing events with no negative center of mass velocities and crosses representing events with negative center of mass velocities. The scale for the sea surface elevation is the typical water depth $H = 2000\,\mathrm{m}$, and Fr is the maximum horizontal velocity of the center of mass scaled with the linear wave speed $\sqrt{gH}$. The power law fits apply to η_{min} with x representing the x-axes. 22

Fig. 12 Scaled maximum and absolute minimum landward sea surface elevation η_{max} and η_{min} against scaled maximum angular momentum L for (**a**) set S1 and (**b**) set S2. The scale for the sea surface elevation is the typical water depth $H = 2000\,\mathrm{m}$, and the scale for the angular momentum is the slump's density ρ_d times the square root of the linear wave speed $\sqrt{gH}$ times the 4^{th} power of the typical slump thickness $d = 250\,\mathrm{m}$. The power law fits apply to η_{max} with x representing the x-axes. 23

Fig. 13 Snapshots of the landslide thickness for the 1929 Grand Banks over-topping slump scenario at different times. The slump mass over-tops its bounding faults and transforms into a translational landslide as Schulten et al. (2019b) propose. The employed BingClaw parameters are $\tau_y = 85\,\mathrm{kPa}$, $\mu = 10\,\mathrm{kPa\,s}^n$, and $n = 0.25$. 23

Fig. 14 Snapshots of the spreading waves for the 1929 Grand Banks over-topping slump source shown in Figure 13. Land is represented by green colour. 24

Fig. 15 Maximum sea surface elevation until $8\,h\,20\,min$ in a transect (see Figure 1) near the Burin Peninsula for three different sediment yield strengths τ_y, and for both (**a**) the 1929 Grand Banks over-topping slump and (**b**) the 1929 Grand Banks pure slump. Other employed BingClaw parameters for both slump events are $\mu = 10\,\mathrm{kPa\,s}^n$ and $n = 0.25$. The water depth along this transect is between 20 m and 50 m. 24

Fig. 16 Maximum sea surface elevation until $8\,h\,20\,min$ for the total wave field for (**a**) the 1929 Grand Banks over-topping slump and (**b**) the 1929 Grand Banks pure slump. The employed BingClaw parameters are $\tau_y = 85\,\mathrm{kPa}$, $\mu = 10\,\mathrm{kPa\,s}^n$, and $n = 0.25$. Land is represented by green colour. 25

Fig. 17 Snapshots of the slump thickness for the 1929 Grand Banks pure slump scenario at different times. The slump mass stays inside the source area with employed BingClaw parameters $\tau_y = 85\,\mathrm{kPa}$, $\mu = 10\,\mathrm{kPa\,s}^n$, and $n = 0.25$. 25

Fig. 18 Snapshots of the spreading waves for the 1929 Grand Banks pure slump source shown in Figure 17. Land is represented by green colour. 26

List of Tables

Table 1 Default parameters used for the 1HD and 2HD simulations 17

Table 2 Geometrical and geotechnical parameters used for the 1HD simulations. The bold values are also used for the 2HD simulations 17

Table 3 Numerical parameters for the 1HD grid refinement tests 18

Table 4 Numerical parameters for the 2HD grid refinement tests 19

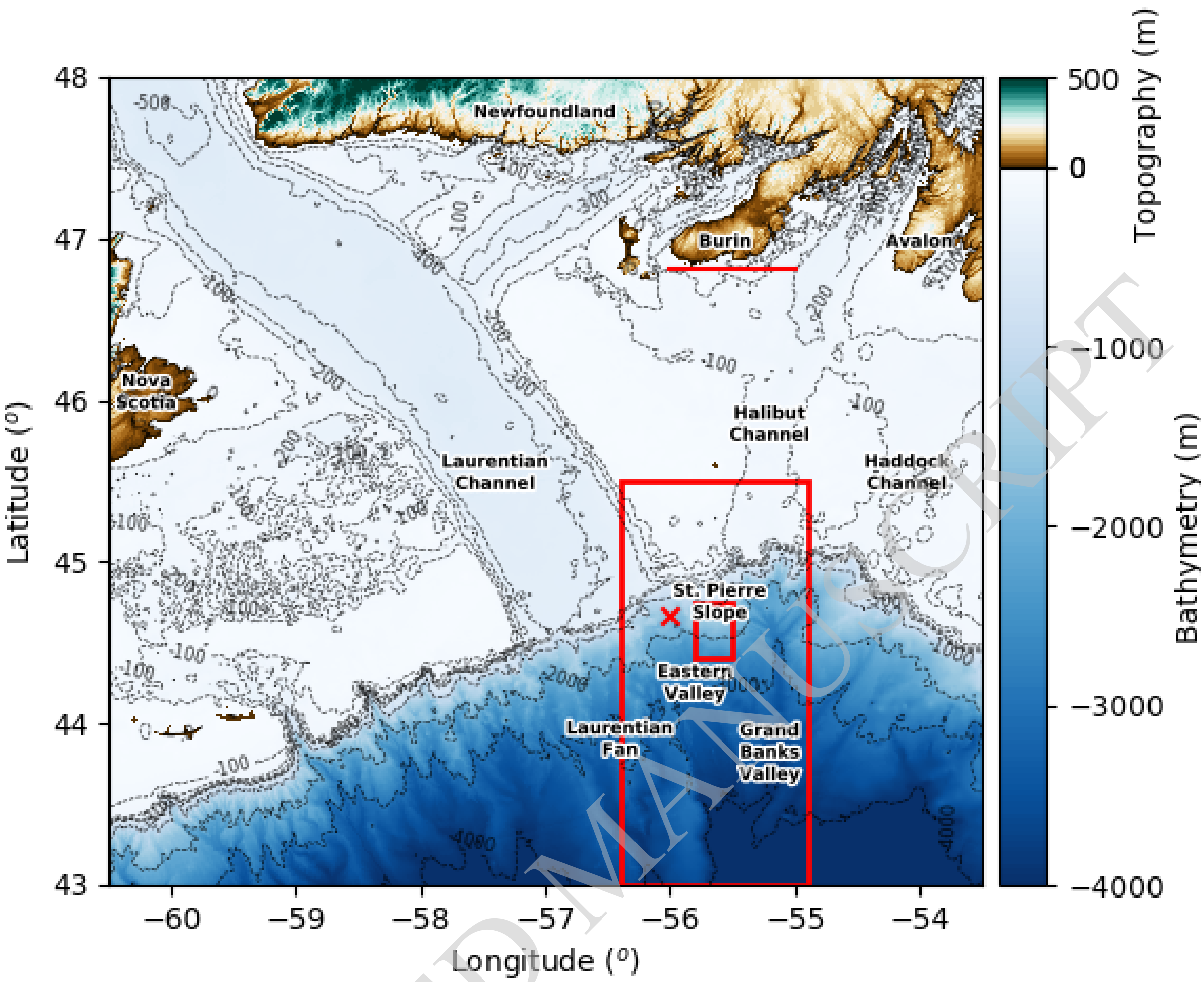

Fig. 1. Bathymetric map of the computational domain for the 2HD tsunami simulations. The bathymetry inside the large red rectangle is used for the simulation of the 2HD landslide dynamics and the small red rectangle is the slump source area. The red line just south of the Burin Peninsula represents the transect that is used to extract simulation results shown in Figure 15. The red cross shows the epicenter of the M_w 7.2 earthquake on 8 November 1929.

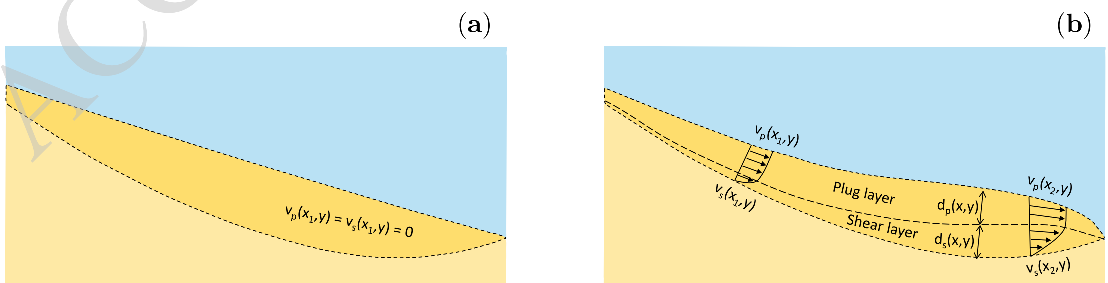

Fig. 2. Simplified schematic plot of the velocity profile (**a**) before and (**b**) during the slump motion simulated with the depth-averaged BingClaw model (modified after Kim et al. (2019) for our slump model). The velocity profile is uniform in the plug layer, but follows a power-law with exponent $n + 1$ in the bottom shear layer. Velocities v_p and v_s, and thicknesses d_p and d_s vary spatially and temporally.

Table 1. *Default parameters used for the 1HD and 2HD simulations*

Parameter	Symbol	Value	Units
Sea water density	ρ_w	1000	$\mathrm{kg\,m^{-3}}$
Landslide density	ρ_d	2000	$\mathrm{kg\,m^{-3}}$
Gravitational acceleration	g	9.81	$\mathrm{m\,s^{-2}}$
Added-mass coefficient	C_m	0.1	-
Skin friction coefficient	C_F	0.001	-
Pressure drag coefficient	C_P	0.25	-

Table 2. *Geometrical and geotechnical parameters used for the 1HD simulations. The bold values are also used for the 2HD simulations*

Parameter	Symbol	Values								Units
Slump volume per unit width	A	1.7	2.9	4.0	5.2	6.3	7.5			$\mathrm{km^2}$
Slump surface slope angle	θ	1	1.5	2	**2.5**	3	3.5			°
Yield strength	τ_y	10	**25**	40	**55**	70	**85**	100	115	kPa
Herschel-Bulkley flow exponent	n	0.1	**0.25**	0.5	0.75	1.0				-
Dynamic landslide consistency	μ	1	4	7	**10**	13	16			$\mathrm{kPa\,s}^n$

Set S1 with a constant volume per unit width $A = 5.2\,\mathrm{km^2}$ and set S2 with a constant slump surface slope angle $\theta = 2.5°$ each combine to 1440 scenarios.

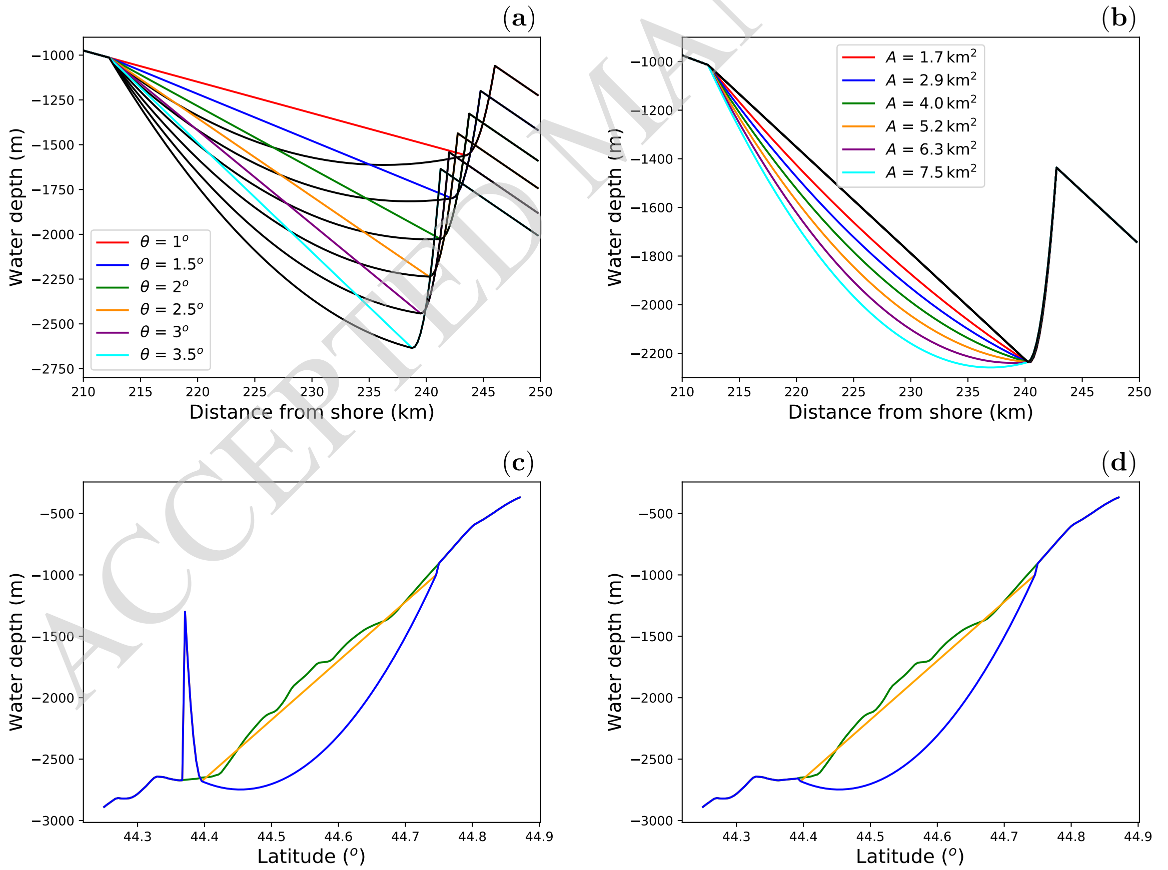

Fig. 3. Initial 1HD bathymetry with slump masses for (**a**) set S1 and (**b**) set S2. Bathymetry with orange lines indicate the same geometrical setup. Transects through longitude −55.77° over the initial 2HD bathymetry for (**c**) the pure slump that includes side walls and a bottom wall, and (**d**) the over-topping slump. The orange line indicates the initial slump surface and the blue line the seabed for the simulations. The green line represents the seabed surface prior to excavation.

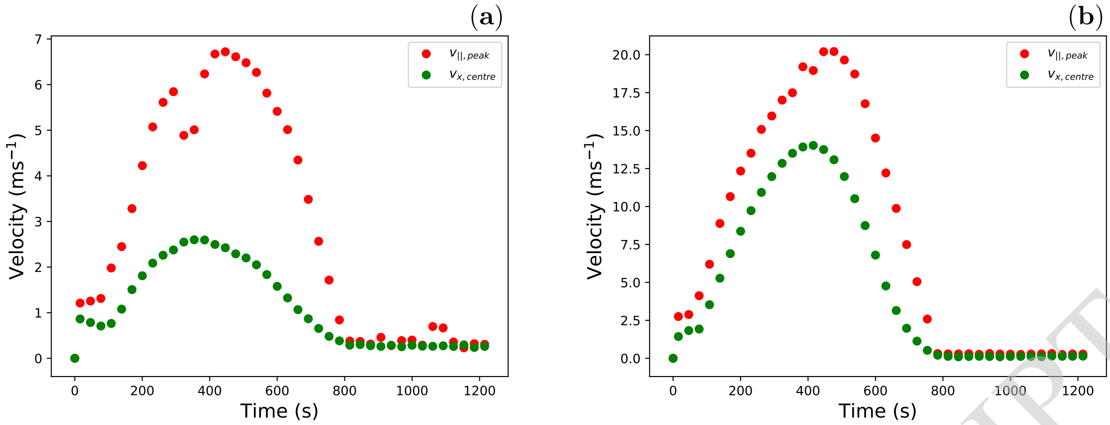

Fig. 4. Time series of center of mass velocity $v_{x,centre}$ and peak bed-parallel velocity over the entire slump body $v_{||,peak}$. Maximum velocities are used for further analyses. Employed parameters are $\mu = 10\,\mathrm{kPa\,s}^n$, $n = 0.25$, the slump surface slope angle is $\theta = 2.5°$, the slump volume per unit width is $A = 5.2\,\mathrm{km}^2$, and (**a**) $\tau_y = 70\,\mathrm{kPa}$, (**b**) $\tau_y = 40\,\mathrm{kPa}$.

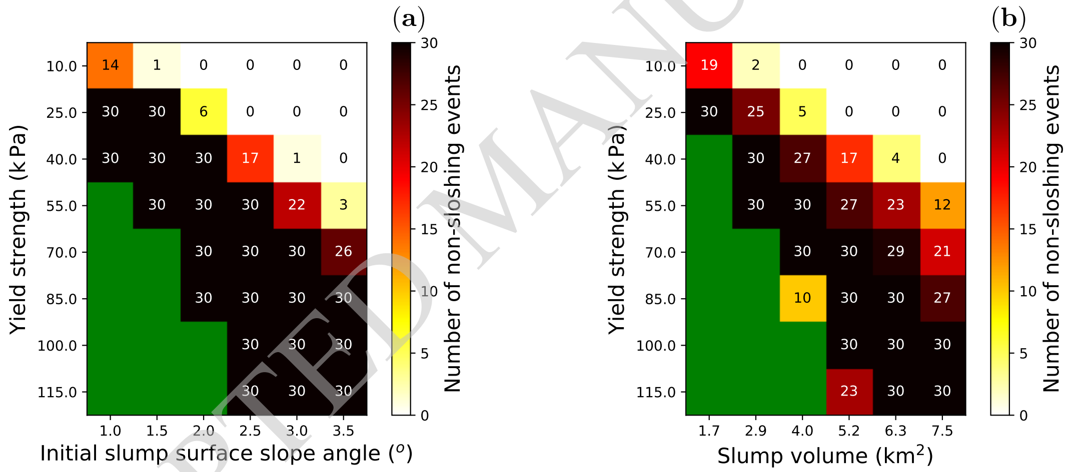

Fig. 5. Number of non-sloshing events and events with velocities greater than zero as a function of yield strength τ_y, (**a**) initial slump surface slope angle θ and (**b**) slump volume per unit width A. All combinations of flow exponent n and dynamic viscosity μ combine to a total of 30 events. Low τ_y, large A, and large θ indicate sloshing events. Large τ_y, low A, and low θ indicate stable sediments and are coloured in green.

Table 3. *Numerical parameters for the 1HD grid refinement tests*

Physical process	Numerical parameter	Value
Landslide	cell size	26.7 m, 40 m, **80 m**, 160 m
Landslide	CFL number	**0.45**
Kajiura type filter	time interval	5 s, 10 s, 15 s, 20 s, **30 s**, 40 s, 50 s, 60 s
Kajiura type filter	cell size	**80 m**
Wave propagation	cell size	55 m, 110 m, **220 m**
Wave propagation	CFL number	**0.5**

Applied models are BingClaw, Kajiura filter, and GloBouss in 1HD. We used the values in bold for our study.

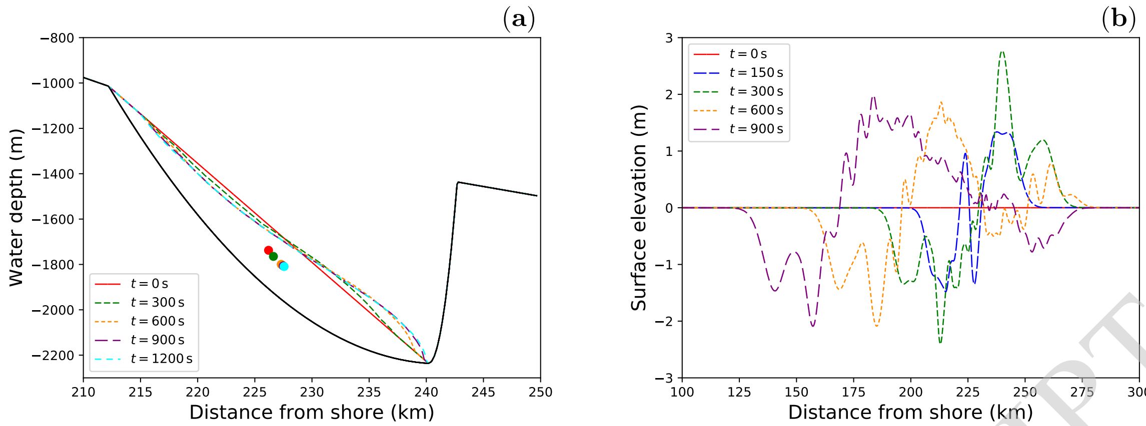

Fig. 6. (**a**) Simulated submarine slump shown for different times. The employed BingClaw parameters are $\tau_y = 70$ kPa, $\mu = 10$ kPa s^n, $n = 0.25$, the slump surface slope angle is $\theta = 2.5°$, and the slump volume per unit width is $A = 5.2\,\text{km}^2$. We show the slump from its initial state until it stops moving, 1200 s after failure. The dots indicate the center of mass of the slump as a function of time; (**b**) tsunami-genesis and propagation until 900 s, which is the time we evaluate the maximum and absolute minimum landward sea surface elevation. The offshore going wave has been relaxed by the sponge layer at the right boundary starting at 250 km from the shore.

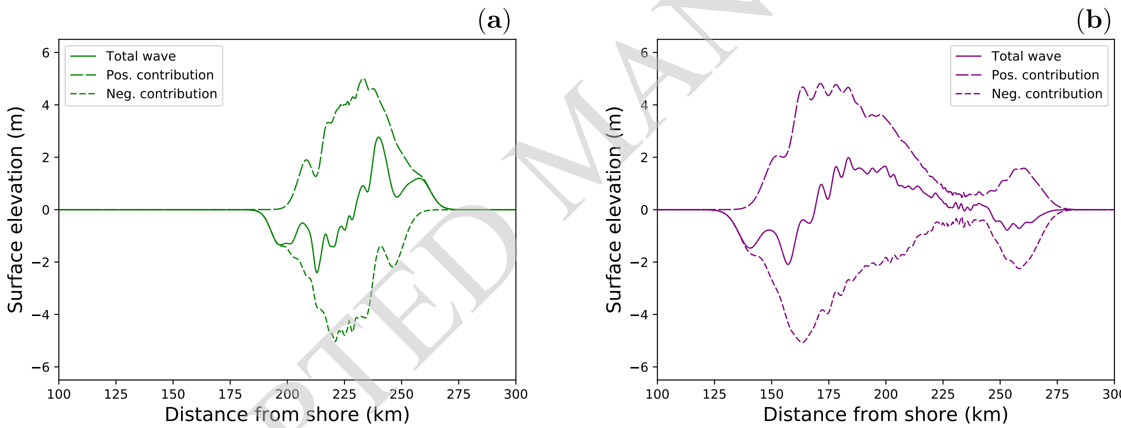

Fig. 7. Tsunami split into the total wave (in solid lines), due to slump uplifts (in long dashed lines) and slump depressions (in short dashed lines). Elapsed times are (**a**) 300 s and (**b**) 900 s. The latter time is when we evaluate the maximum and absolute minimum landward sea surface elevation. The offshore going wave has been relaxed by the sponge layer at the right boundary starting at 250 km from the shore.

Table 4. *Numerical parameters for the 2HD grid refinement tests*

Physical process	Numerical parameter	Value
Landslide	cell size	93 m, **185 m**, 370 m, 741 m, 1482 m
Landslide	CFL number	0.45, **0.65**, 0.85
Kajiura type filter	time interval	20 s, **30 s**, 50 s, 80 s, 300 s
Kajiura type filter	cell size	232 m, **463 m**, 926 m
Wave propagation	cell size	**463 m**, 926 m, 1852 m
Wave propagation	CFL number	0.4, 0.6, **0.8**, 1.0

Applied models are BingClaw, Kajiura filter, and GloBouss in 2HD. We used the values in bold for our study.

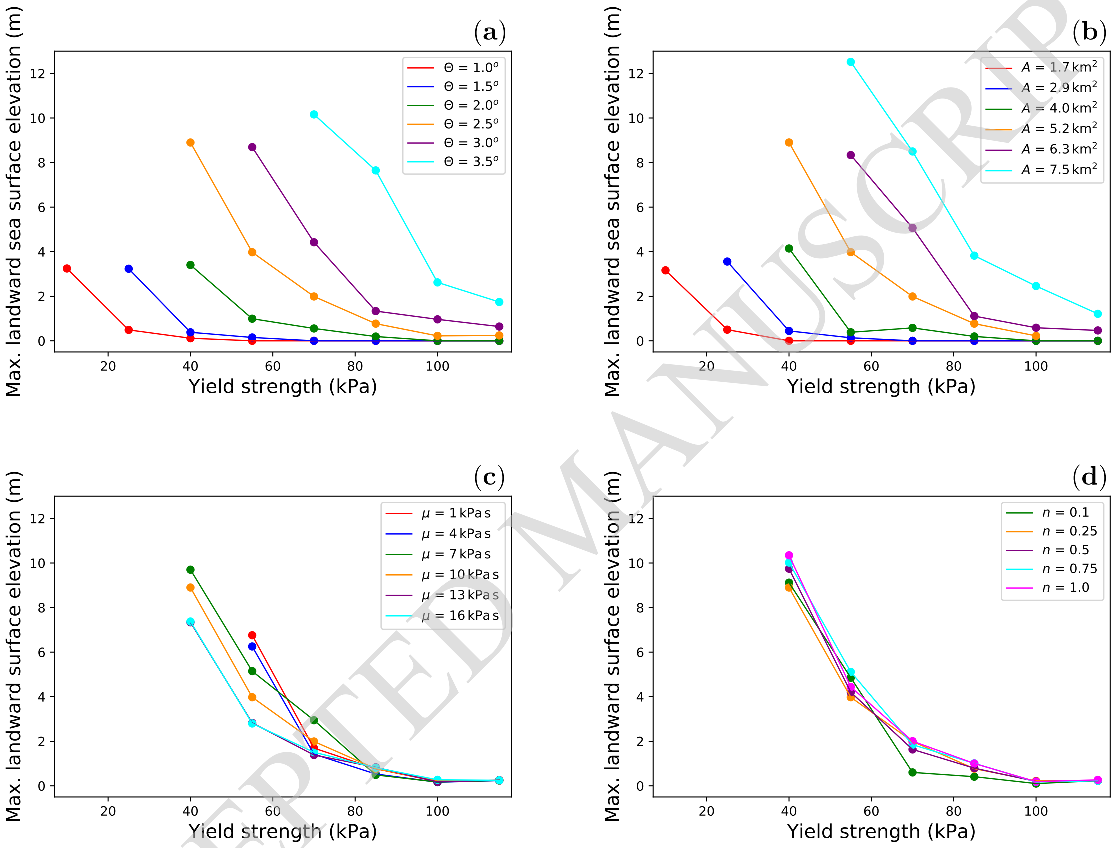

Fig. 8. Maximum landward sea surface elevations η_{max} as a function of yield strength τ_y for a selection from (**a**) set S1, (**b**) set S2, and (**c**,**d**) common scenarios from both sets. Orange lines in all subplots refer to the same scenarios. Fixed parameters (except where parameters are subject to variation) are $\mu = 10\,\mathrm{kPa\,s}^n$, $n = 0.25$, $\theta = 2.5°$, and $A = 5.2\,\mathrm{km}^2$.

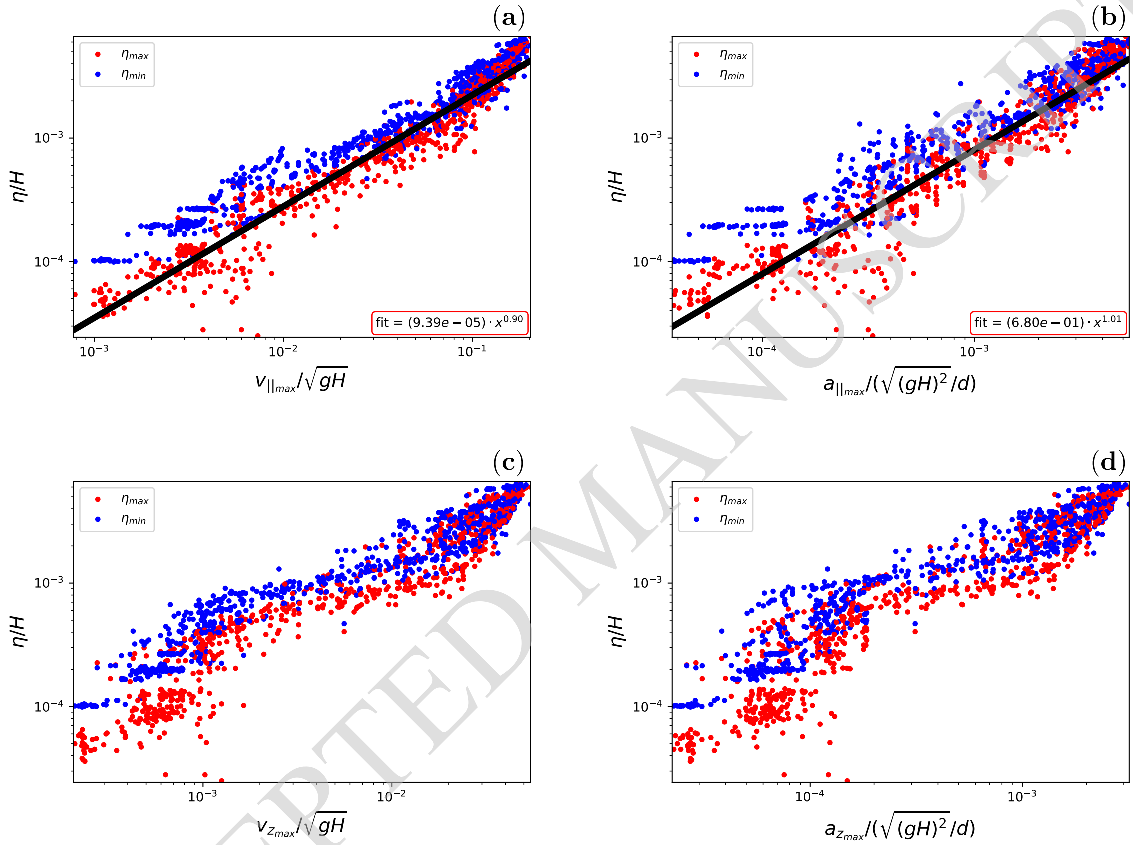

Fig. 9. Scaled maximum and absolute minimum landward sea surface elevation η_{max} and η_{min} against (**a**) scaled maximum bed-parallel slump velocity $v_{||_{max}}$, (**b**) scaled maximum bed-parallel slump acceleration $a_{||_{max}}$, (**c**) scaled maximum vertical slump velocity $v_{z_{max}}$, and (**d**) scaled maximum vertical slump acceleration $a_{z_{max}}$ for set S1. The scale for the sea surface elevation is the typical water depth $H = 2000\,$m, the velocity scale is the linear wave speed $\sqrt{gH}$, and the acceleration scale is the square linear wave speed $\sqrt{gH}$ divided by the typical slump thickness $d = 250\,$m. The power law fits apply to η_{max} with x representing the x-axes.

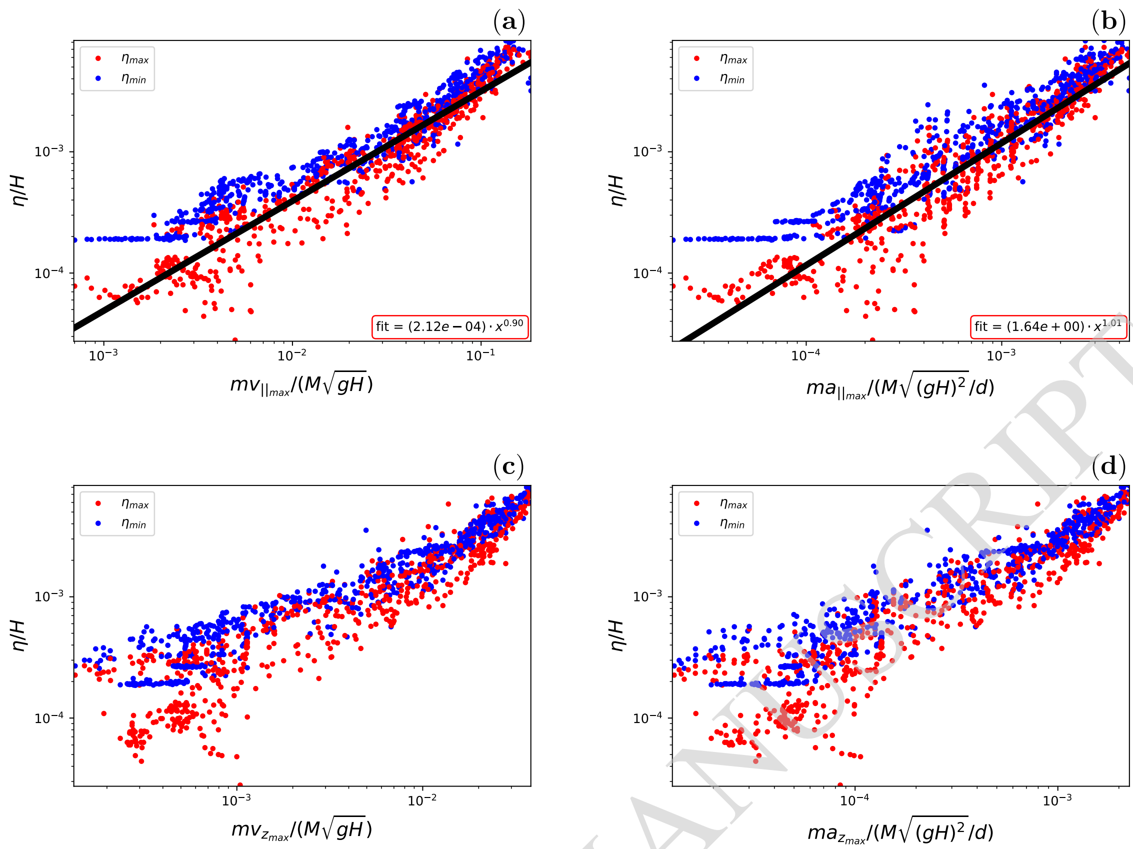

Fig. 10. Scaled maximum and absolute minimum landward sea surface elevation η_{max} and η_{min} against (**a**) scaled maximum bed-parallel slump momentum $m\,v_{||_{max}}$, (**b**) scaled maximum bed-parallel slump momentum rate $m\,a_{||_{max}}$, (**c**) scaled maximum vertical slump momentum $m\,v_{z_{max}}$, and (**d**) scaled maximum vertical slump momentum rate $m\,a_{z_{max}}$ for set S2. The scale for the sea surface elevation is the typical water depth $H = 2000\,\mathrm{m}$, the momentum scale is the largest mass M (from the $A = 7.5\,\mathrm{km}^2$ scenarios) times the linear wave speed $\sqrt{gH}$, and the scale for the momentum rate is the largest mass M times the square linear wave speed $\sqrt{gH}$ divided by the typical slump thickness $d = 250\,\mathrm{m}$. The power law fits apply to η_{max} with x representing the x-axes.

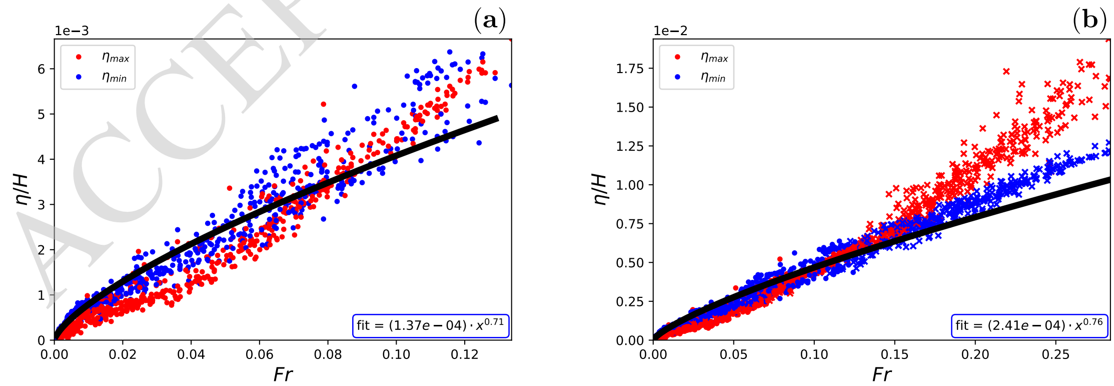

Fig. 11. Scaled maximum and absolute minimum landward sea surface elevation η_{max} and η_{min} as a function of the Froude number Fr for set S1, with (**a**) filtered events only and (**b**) unfiltered events with dots representing events with no negative center of mass velocities and crosses representing events with negative center of mass velocities. The scale for the sea surface elevation is the typical water depth $H = 2000\,\mathrm{m}$, and Fr is the maximum horizontal velocity of the center of mass scaled with the linear wave speed $\sqrt{gH}$. The power law fits apply to η_{min} with x representing the x-axes.

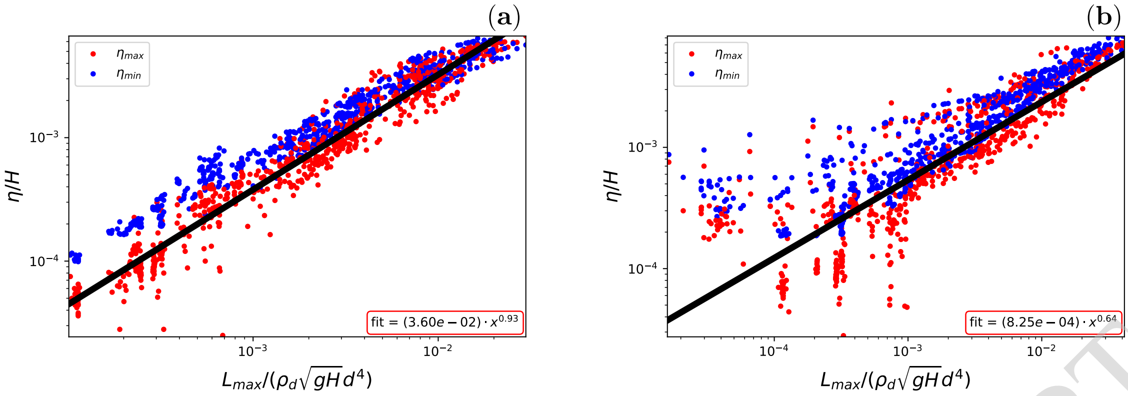

Fig. 12. Scaled maximum and absolute minimum landward sea surface elevation η_{max} and η_{min} against scaled maximum angular momentum L for (**a**) set S1 and (**b**) set S2. The scale for the sea surface elevation is the typical water depth $H = 2000\,\mathrm{m}$, and the scale for the angular momentum is the slump's density ρ_d times the square root of the linear wave speed $\sqrt{gH}$ times the 4^{th} power of the typical slump thickness $d = 250\,\mathrm{m}$. The power law fits apply to η_{max} with x representing the x-axes.

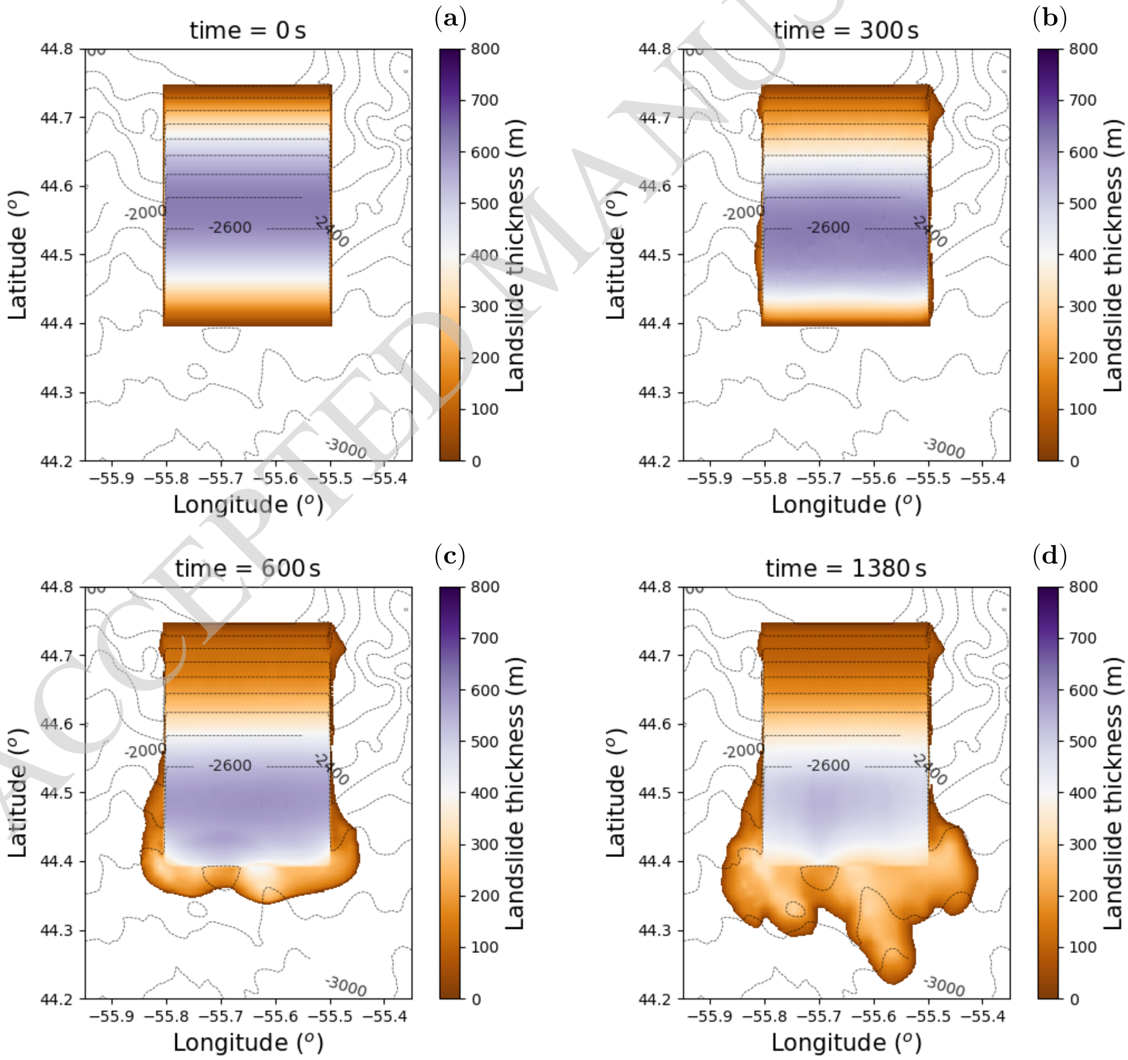

Fig. 13. Snapshots of the landslide thickness for the 1929 Grand Banks over-topping slump scenario at different times. The slump mass over-tops its bounding faults and transforms into a translational landslide as Schulten et al. (2019b) propose. The employed BingClaw parameters are $\tau_y = 85\,\mathrm{kPa}$, $\mu = 10\,\mathrm{kPa\,s}^n$, and $n = 0.25$.

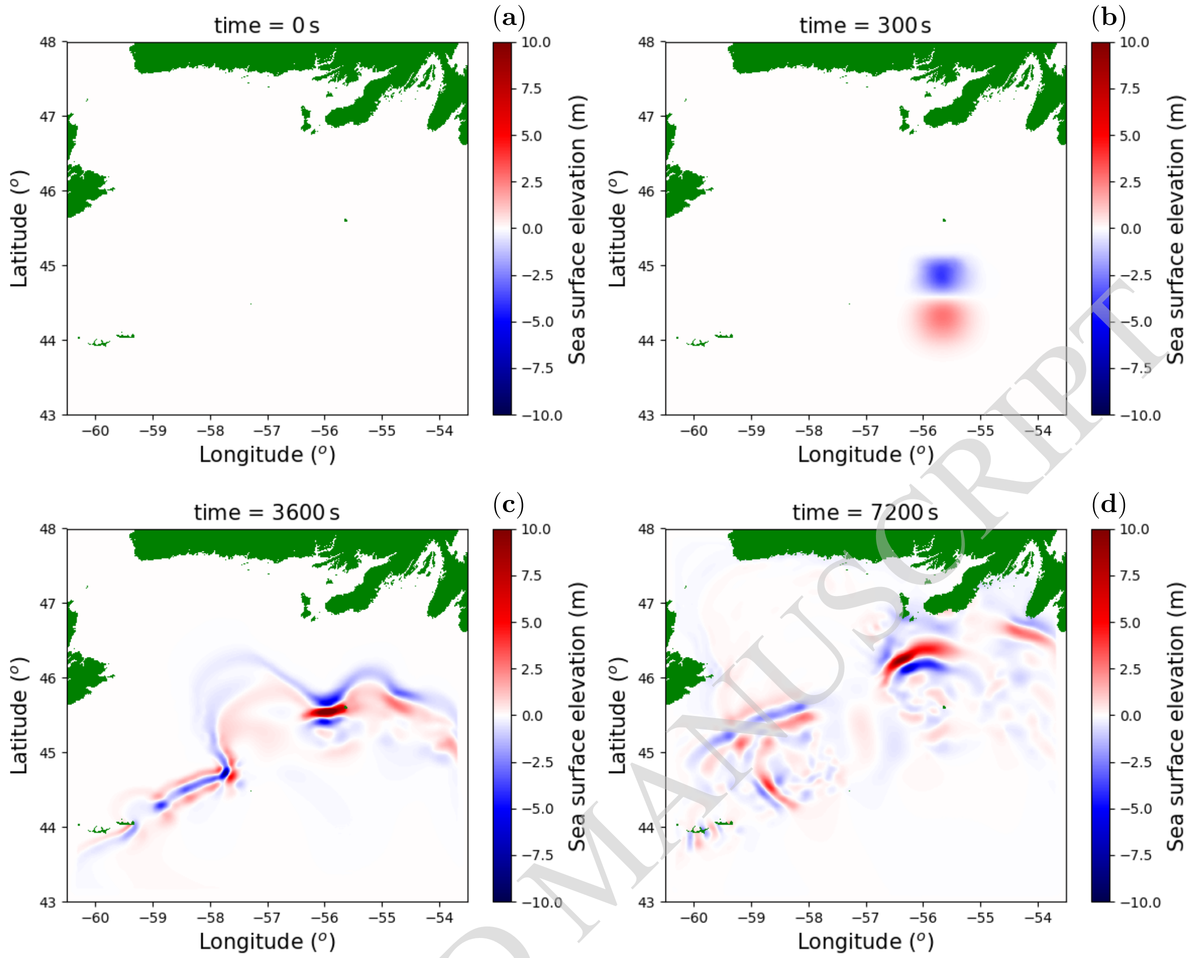

Fig. 14. Snapshots of the spreading waves for the 1929 Grand Banks over-topping slump source shown in Figure 13. Land is represented by green colour.

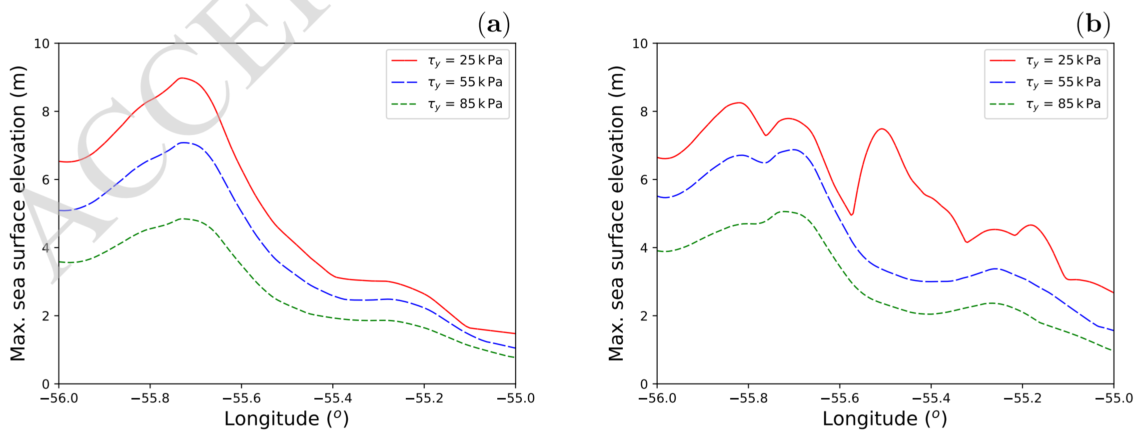

Fig. 15. Maximum sea surface elevation until $8\,h\,20\,min$ in a transect (see Figure 1) near the Burin Peninsula for three different sediment yield strengths τ_y, and for both (**a**) the 1929 Grand Banks over-topping slump and (**b**) the 1929 Grand Banks pure slump. Other employed BingClaw parameters for both slump events are $\mu = 10\,\mathrm{kPa\,s}^n$ and $n = 0.25$. The water depth along this transect is between 20 m and 50 m.

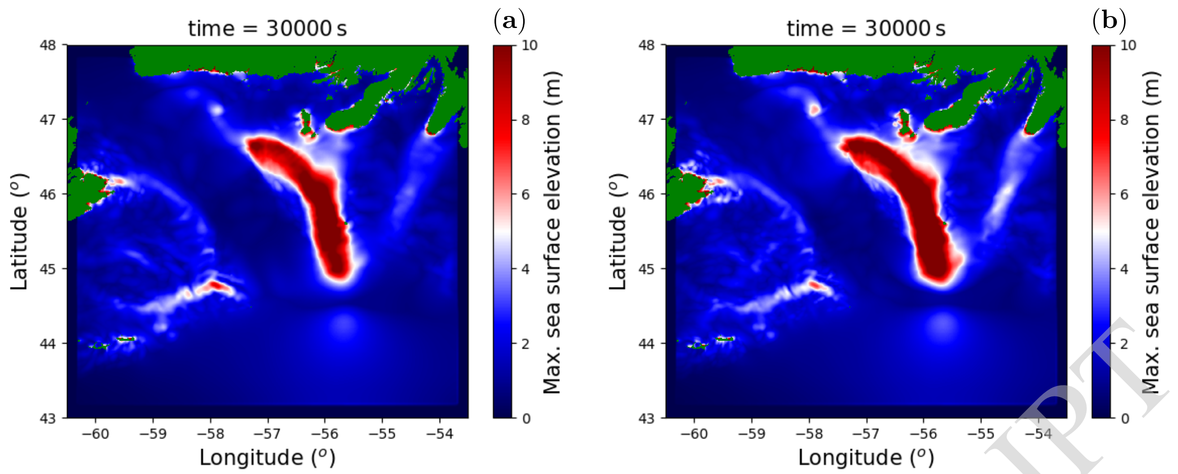

Fig. 16. Maximum sea surface elevation until $8\,h\,20\,min$ for the total wave field for (**a**) the 1929 Grand Banks over-topping slump and (**b**) the 1929 Grand Banks pure slump. The employed BingClaw parameters are $\tau_y = 85\,\mathrm{kPa}$, $\mu = 10\,\mathrm{kPa\,s}^n$, and $n = 0.25$. Land is represented by green colour.

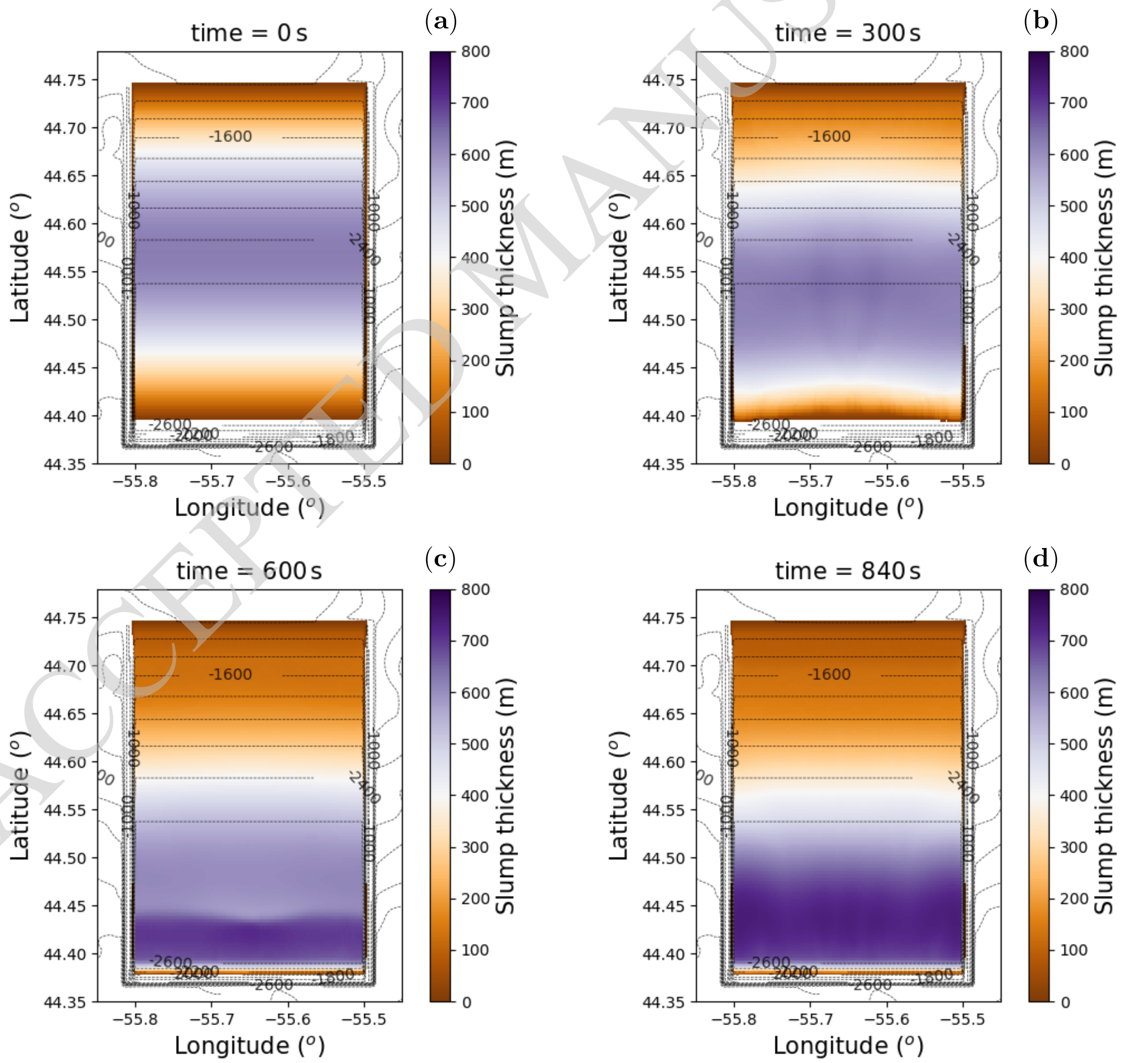

Fig. 17. Snapshots of the slump thickness for the 1929 Grand Banks pure slump scenario at different times. The slump mass stays inside the source area with employed BingClaw parameters $\tau_y = 85\,\mathrm{kPa}$, $\mu = 10\,\mathrm{kPa\,s}^n$, and $n = 0.25$.

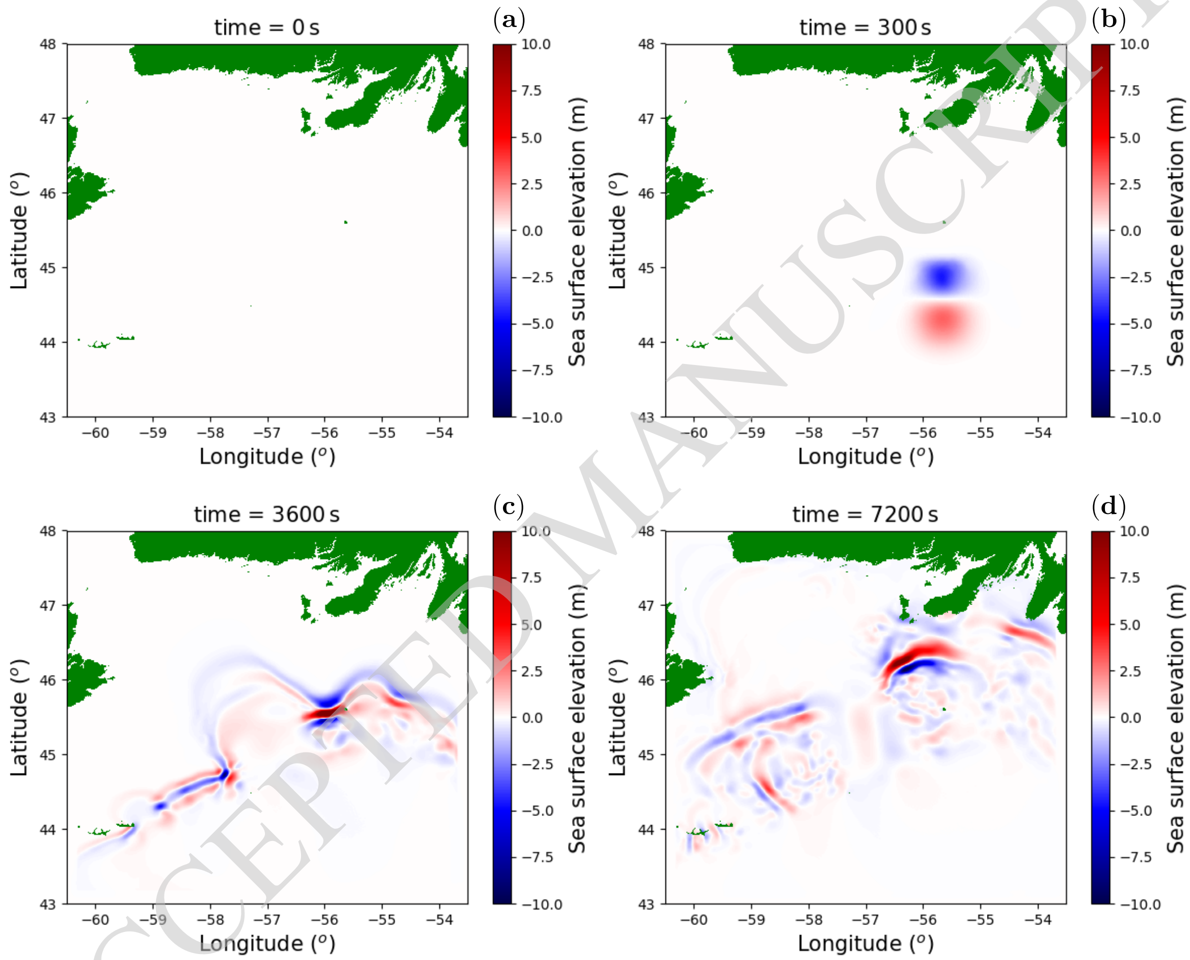

Fig. 18. Snapshots of the spreading waves for the 1929 Grand Banks pure slump source shown in Figure 17. Land is represented by green colour.